National Library
of Canada

Acquisitions and
Bibliographic Services Branch

395 Wellington Street
Ottawa, Ontario
K1A 0N4

Bibliothèque nationale
du Canada

Direction des acquisitions et
des services bibliographiques

395, rue Wellington
Ottawa (Ontario)
K1A 0N4

Your file Votre référence

Our file Notre référence

NOTICE

The quality of this microform is heavily dependent upon the quality of the original thesis submitted for microfilming. Every effort has been made to ensure the highest quality of reproduction possible.

If pages are missing, contact the university which granted the degree.

Some pages may have indistinct print especially if the original pages were typed with a poor typewriter ribbon or if the university sent us an inferior photocopy.

Reproduction in full or in part of this microform is governed by the Canadian Copyright Act, R.S.C. 1970, c. C-30, and subsequent amendments.

AVIS

La qualité de cette microforme dépend grandement de la qualité de la thèse soumise au microfilmage. Nous avons tout fait pour assurer une qualité supérieure de reproduction.

S'il manque des pages, veuillez communiquer avec l'université qui a conféré le grade.

La qualité d'impression de certaines pages peut laisser à désirer, surtout si les pages originales ont été dactylographiées à l'aide d'un ruban usé ou si l'université nous a fait parvenir une photocopie de qualité inférieure.

La reproduction, même partielle, de cette microforme est soumise à la Loi canadienne sur le droit d'auteur, SRC 1970, c. C-30, et ses amendements subséquents.

Canada

EFFECTS OF SOLUTE POLARIZATION ON THE HYDRODYNAMICS WITHIN MEMBRANE-FLUID-SOLUTE SYSTEMS, WITH SPECIAL APPLICATION TO HOLLOW FIBER BIOREACTORS

by

Sumita Bhola

A thesis submitted to the school of Graduate Studies and Research in partial fulfillment of

the requirements for the degree of

MASTER OF APPLIED SCIENCE

in the Department of Chemical Engineering

University of Ottawa

June, 1994

National Library of Canada
Acquisitions and Bibliographic Services Branch
395 Wellington Street
Ottawa, Ontario
K1A 0N4

Bibliothèque nationale du Canada
Direction des acquisitions et des services bibliographiques
395, rue Wellington
Ottawa (Ontario)
K1A 0N4

Your file Votre référence

Our file Notre référence

ISBN 0-612-00449-X

Canada

UNIVERSITÉ D'OTTAWA
UNIVERSITY OF OTTAWA

ABSTRACT

The application of bioprocessing schemes has become important in the production of biological molecules, including pharmaceuticals which play key roles in the areas of diagnostics and the prevention and treatment of diseases. Membrane bioreactors such as the hollow fiber bioreactor are effective at immobilizing cells during bioproduction. However, a potential problem with hollow fiber bioreactors is the presence of concentration gradients in nutrients, wastes and products in the extracapillary space which subject cells to varying local conditions. These gradients should be minimized or, preferably, eliminated.

The primary objective of this study was to assess the influence of osmotically active macromolecules on the hydrodynamics of hollow fiber membrane systems which, in turn, influences solute distributions within these bioreactors. This included verifying the phenomenon of concentration polarization of bovine serum albumin (BSA) in a rectilinear flow cell designed to incorporate the salient features of the hollow fiber bioreactor. Following characterization of the membrane used in the study, experimentally determined concentration profiles of BSA were compared with those predicted from theoretical analysis.

The membrane characterization revealed local variability in the permeability of the membrane: L_p/μ was found to vary between 2.80×10^{-11} and 8.19×10^{-11} m^2s/kg. The membrane permeability did not exhibit hysteresis effects due to pressure nor were there substantial changes in the permeability as a result of membrane aging. The permeability of the membrane decreased by approximately 30% following conditioning with a solution of BSA and was successful at retaining the protein.

Transient BSA polarization was observed in the extra-luminal space of the rectilinear flow cell after 12, 24 and 36 hours of operation. The theoretical concentration profiles of BSA over predicted the experimental concentration profiles when assuming a

membrane permeability equal to the average of the membrane coupon measurements. Therefore, further experiments were pursued in an attempt to resolve the discrepancy between the theoretical and experimental results. These experiments consisted of examining possible dilution of the BSA samples obtained from the flow cell as well as investigating the theoretical assumption of a one-dimensional model. Sedimentation experiments showed that settling of the protein was not responsible for diluting the BSA samples. The local variability in the membrane permeability is thought to contribute to the discrepancy between the theoretical and experimental concentration profiles, as well as transverse concentration gradients not considered by the model.

ACKNOWLEDGMENTS

The successful completion of this research project was due to several people. I am indebted to my research supervisor Dr. Taylor for his support, understanding and kindness throughout this challenging project. His guidance and constructive criticism served well from the initial planning stages to the completion of the thesis. I would further like to thank Dr. Taylor for the interesting conversations which I enjoyed a great deal.

I am also grateful to Mr. Louis Tremblay for his invaluable contribution in the design of the flow cell. In addition to his technical assistance, he provided me with support and encouragement during the difficult phases of the project. I would like to take the opportunity to thank Dr. A. Tremblay for his interest in my project and his valued advice, especially concerning the membrane characterization. He devoted a great deal of time to help me overcome the inherent difficulties of this project. I am grateful to Mr. Karol Lacki for his assistance with the Millennium software and the HPLC system.

Finally, I am indebted to Mr. Dev Manku for his continued support during this research project. The successful completion of this project is owed to his generosity and convictions which inspired me. His assistance and encouragement served to keep me in good spirits. Also, I would like to take this opportunity to thank my parents, my sister and my brother for their understanding and patience during my academic career.

NOMENCLATURE

a	One-half the chamber width, m
b	One-half the chamber height, m
B	Width of the upper and lower chambers, m
C	Concentration, kg/L
D	Protein diffusion coefficient, m^2/s
H_1	Height of the lower chamber, m
H_2	Total height of the upper and lower chambers, m
L	Chamber length, m
L_p	Membrane permeability, m
k	Darcy permeability, m^2
M_p	Molecular weight of protein, kg/kmol
P	Pressure, kPa
Q	Volumetric flow rate, m^3/s
R	Gas constant, J/mol K
T	Temperature, K
t	Time, s
u	Fluid velocity, m/s
V	Superficial velocity, m/s

Greek Symbols

μ	Fluid viscosity, kg/ms
Π	Osmotic pressure, kPa

Subscripts

L	Denotes lower chamber
E	Denotes upper chamber
M	Denotes membrane
o	Denotes inlet

Superscripts

max	Denotes maximum value

CONTENTS

Appendices

LIST OF TABLES

LIST OF FIGURES

1. INTRODUCTION

1.1 Importance of Bioprocessing

The application of bioprocessing schemes, as opposed to synthetic chemical methods, has become important in the production of biological molecules, especially pharmaceuticals. Bioprocessing is used in the formation of complex molecules such as viral vaccines and in the conversion of a particular isomer from a racemic mixture. Complex mammalian proteins, including hormones, antibodies and viruses play key roles in areas such as diagnostics, prevention and treatment of diseases (Belfort, 1989). The medicinal value of proteins essential to human healthcare is exemplified by the human growth hormone used to treat hypopituitary dwarfism and by monoclonal antibodies considered for targeted treatment of cancer. Traditionally, the source of mammalian proteins has been from placenta, cadavers and the plasma of blood donors. However, these sources tend to be limited, and the current fear of viral contamination with HIV, hepatitis, etc. further fuels the large scale industrial production of such proteins and reinforces the importance of bioprocessing (Piret and Cooney, 1990a). The need for reactor configurations and conditions which render a high yield of valuable concentrated biologicals provides the motivation for research in this field (Schonberg and Belfort, 1987).

Culturing animal, plant, yeast and insect cells for the ultimate production of complex biological molecules is achieved by numerous entrapment technologies (Heath et al., 1990; Piret et al., 1991). One method of immobilizing cells is to attach or sorb the cells onto a surface. Other methods involve the entrapment of cells within porous matrices such as polysaccharide gels and ceramics, or the entrapment behind a barrier such as a membrane. Membrane bioreactors are particularly effective for immobilizing whole cells and enzymes. Further, the permselective properties of the membrane can favour *in* *situ* separation of the product (Belfort, 1989). Proteins such as blood clotting factors, human growth factors, interferons and monoclonal antibodies are currently being studied and methods to manufacture them competitively provide a major impetus for further development of membrane bioreactors such as the hollow fiber bioreactor.

The present work focuses on operational aspects of hollow fiber bioreactors, namely, the improvement of bioreactor efficiency by virtue of investigating concentration gradients in the immobilized region. Background information will first be provided prior to outlining the research objectives which appear at the end of Chapter 1.

1.2 The Hollow Fiber Bioreactor

Various flow configurations can be achieved for hollow fiber modules. Although all geometries of the hollow fiber reactor are subject to the same physical principles, the precise configuration influences the pressure drop and the magnitude and direction of flows (Bruining, 1989). Prior work has focused on configurations such as slits, tubes, annuli, porous ducts and spiral wound membrane modules. In particular, the closed-shell mode, which seeks to limit convective flows to within the fiber lumen, has been the most popular configuration studied thus far (Kelsey et al., 1990).

The classical hollow fiber cartridge is composed of a bundle of fibers encompassed by a cylindrical casing acquiring the likes of a shell-and-tube heat exchanger (Kelsey et al., 1990). A bundle may consist of hundreds or even thousands of fibers (Novais, 1985; Park and Chang, 1986). Fiber lengths range from a few centimeters to several meters. Each fiber is small with an internal diameter on the order of 200μm. The fibers are typically spaced 100-300 μm apart, accommodating 15-25 layers of cells (Cherry, 1989). Commonly used hollow fiber membranes include polysulfone, cellulose acetate and polypropylene. The fibers may be anisotropic or isotropic. Anisotropic fibers are characterized by a thin membrane layer surrounded by a porous support. Bioseparation occurs at the thin membrane layer which is 1-2 μm thick. The porous support is typically 50-75 μm thick and provides physical support for the membrane layer (Tharakan and Chau, 1986). A typical anisotropic hollow fiber is illustrated in Figure 1.1. Isotropic membranes, on the other hand, can be porous or dense but the membrane permeability remains constant and uniform in all directions (Baker, 1991).

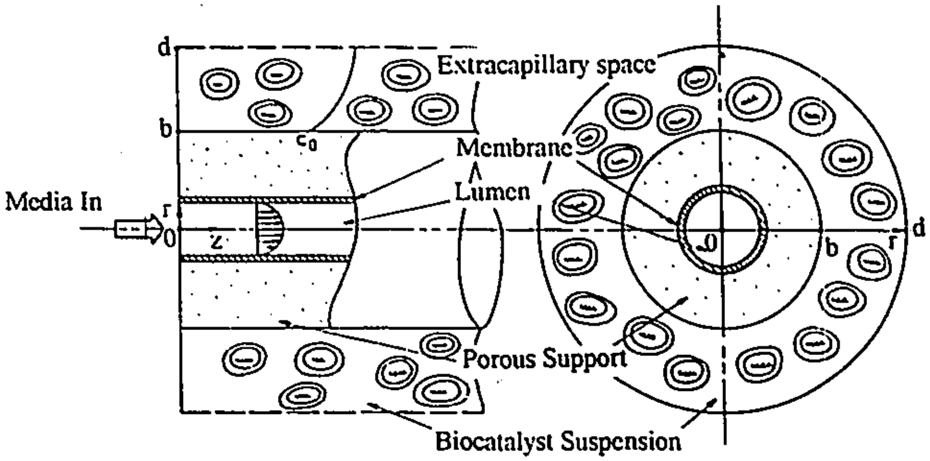

Figure 1.1. Schematic representation of a single hollow fiber (adapted from Heath and Belfort, 1987).

The fibers of these reactors are arranged parallel to each other and are joined to a manifold at each end (Cherry, 1989). The nutrient medium is supplied through the lumen from where essential nutrients such as glucose and glutamine are free to permeate the membrane by diffusion into the extracapillary space (ECS) or shell space. Cells introduced into the ECS are then nourished. Since the hollow fiber is equipped with a semi-permeable membrane, exchange of material between lumen and shell is limited; only certain byproducts of cellular activity, such as CO_2 and lactate, may diffuse from the shell side to the lumen. Others are retained in the ECS. Of course, the particular set of species exchanged depends upon the characteristics of the membrane (Heath and Belfort, 1987).

The ECS is typically occupied by cells capable of producing valuable byproducts.

Some examples displaying the variety of mammalian cells cultured in hollow fibers are shown in Table 1.1. In addition to animal cell culturing, the applications of hollow fiber membrane reactors extend to the ultrafiltration of macromolecular solutions during separation processes, resulting in concentration or purification of solutions (Bruining, 1989; Shen and Probstein, 1977). The hollow fiber also finds application as a membrane device in the artificial organs industry. One such example is the artificial lung which permits exchange of gases such as oxygen and carbon dioxide between inhaled air and the bloodstream via a membrane (Leonard, 1986). The bioartificial pancreas has been used to restore insulin delivery in the treatment of diabetes (Pillarella and Zydney, 1990; Kelsey et al., 1990). The hollow fiber bioreactor has also been used in the fermentation of glucose to ethanol with productivities of up to 0.0194 kg/m^3/s (70 g/L/hr). For the case of ethanol production, the hollow fiber system may be used as the sole reactor or in conjunction with a classical fermenter to perform the separation of cells from valuable products (Novais, 1987).

Table 1.1. Mammalian cell types cultured successfully in hollow fiber bioreactors (Heath and Belfort, 1987).

Organism	Tissue, cell type	Organism	Tissue, cell type
Chick	Embryo, Primary Culture	Human	Foreskin, HFF/HR 218
Duck	Embryo, Primary Culture		Pituitary Tumor, Primary Culture
Mouse	Connective Tissue, L-929		Choriocarcinoma, JEG-7
	Embryo, 3T3/SV3T3		Breast Carcinoma, BT-20/HBT-3
	Myeloma/Spleen Hybridoma		B Lymphoma, NC-37
	MammaryTumor,66/67/168/G8H		Colon Adenocarcinoma, LS-174T
Rat	Pituitary Tumor, MtTW5		Colorectal Adenocarcinomas, SW403/480/620/707
	Liver Hepatoma, Reuber H4-11-E		Colon Carcinoma, DLD-1
Hamster	Kidney, BHK-21		Lymphoma, Myeloma, Leukemia, Melanoma, and Colon Carcinoma
	Ovary, Ha-1		Cervical Carcinoma, HeLa
Monkey	Lung, Rhesus Diploid		Lung, WI-38
	Kidney, Vero		Myeloma/Spleen Hybridoma
	Kidney, Rhesus MK-2		Liver Hepatoma, Alexander PLC/PRF/5

1.3 Advantages and Challenges of Bioreactor Systems

The advantages of bioprocesses over synthetic and physical ones are numerous and diverse. Bioprocesses can occur at milder reaction conditions in comparison to synthetic chemical methods. The use of microbial processing for the desulfurization and denitrogenation of heavy oils illustrates an instance where bioprocessing schemes offer milder reaction conditions than traditional catalytic methods, which are characterized by high pressure and high temperature reaction conditions that contribute to increased costs in this latter case. Therefore, operation at milder reaction conditions typical of bioprocesses can curb expenses and represents a distinct advantage over chemical methods (Belfort, 1989).

The advent of recombinant DNA technology further renders bioprocesses attractive in comparison to synthetic chemical processes. Advances in gene splicing enable the synthesis of custom made proteins from microorganisms (Bull et al., 1987). The microorganism *E. coli* has been genetically engineered to produce human insulin, somatostatin and interleukin 2. Furthermore, recombinant DNA technology can aid in increasing product yields by the use of promoters as well as reducing recovery costs by causing the excretion of selective proteins from microorganisms (Belfort, 1989).

Immobilized membrane bioreactors such as the hollow fiber bioreactor have several additional advantages when applied to these bioprocesses and, in particular, to cell culturing. The geometry of membrane bioreactors affords large surface areas per unit volume. This property enforces substrate delivery and waste removal, leading to high cell densities. In this manner, the cells benefit from a continual supply of nutrients while metabolic wastes are removed. Increased cell densities are accompanied by high product concentrations (Heath et al., 1990). The advantage of large surface areas per unit volume is particularly useful for anchorage dependent cells which require attachment to a solid surface. Immobilized membrane bioreactors have the further advantage of reducing the costs of downstream processing. The cost of product purification is one aspect of the downstream processing operation which is greatly reduced by virtue of incorporating membranes that permit selective nutrients into the immobilized phase (Heath et al., 1990). In addition, the mammalian cell membrane lacks rigidity which renders the cell susceptible to lysis due to mechanical stimuli such as hydrodynamic shear. Hydrodynamic shear can be introduced into a bioreactor by agitating the cell suspension and by sparging gas into the bioreactor. Membrane bioreactors are effective at confining mammalian and plant cells to a low shear environment (Prokop and Rosenberg, 1989).

However, the use of bioprocessing schemes instead of synthetic chemical methods may also prove unfavorable due to various problems and challenges. For example, the maintenance of a sterile environment to avoid the risk of contamination is important in the synthesis of valuable biologicals. A sterile environment for the biocatalyst suspension and the nutrient feed medium can be secured in two ways. First of all, the use of aseptic techniques may be necessary while transferring solutions such as the nutrient medium from the glassware to the reactor vessel. The reactor itself must also be sterilized. Secondly, sterilization may be achieved by the addition of growth inhibitors such as anti-bacterial agents. The effect of growth inhibitors on the kinetics of cell proliferation and antibody production is, in some cases, unknown as in the case of hybridoma cells (Harbour et al., 1988). The cost of these energy intensive sterilization requirements and growth inhibitors is one disadvantage associated with the use of bioprocessing schemes.

Another challenge of bioprocessing methods emerges in the downstream processing of complex mixtures (Belfort, 1989). Inherent to the use of microorganisms is the production of several byproducts of cellular metabolism. Secondary products which may be modifications of the main product are frequently synthesized. During the fermentation of penicillin G, closely related compounds such as pentylpenicillin and phenoxymethylpenicillin, differing only in side chain groups from the desired penicillin G, are also formed (Othmer, 1978). The separation of these byproducts from the desired biological may be difficult. In addition, the mere presence of certain byproducts may have deleterious effects on the production of the desired macromolecule due to product inhibition.

Other limitations associated with hollow fiber membrane bioreactors include fouling of the membrane, clogging of hollow fibers and the possible disruption of the fibers due to cell growth or excessive gas production (Belfort, 1989). Membrane fouling is undesirable since it typically causes the permeability of the membrane to decrease. The transfer of substrate from the lumen to the cells located in the extracapillary space is diminished as a consequence of a decrease in membrane permeability (Heath and Belfort, 1987). On a microscopic scale, the immobilized region is heterogeneous which renders it difficult to sample and analyze experimentally. Due to cellular activity, inhibitory metabolites such as lactate and ammonium build up in the immobilized cell phase during consumption of nutrients (Piret & Cooney, 1990). In addition, restricted transport of nutrients (oxygen and products) to and from cells due to high cell densities leads to the risk of developing necrotic regions (Belfort, 1989). In fact, according to Cherry (1989), a major problem with hollow fiber bioreactors is the presence of concentration gradients in the shell space which subject animal and plant cells to varying local conditions.

1.3.1 Polarization and Starling Flow

1.3.1.1 Order of Magnitude Analysis For Solutes of Varying Molecular Weight

Cell viability relies upon successful nourishment of the cells. The delivery of low molecular weight substrates, such as oxygen and glucose, to the cells retained in the ECS of the hollow fiber bioreactor is primarily achieved by diffusion, as indicated by low Peclet numbers characteristic of low molecular weight solutes. In contrast, the Peclet number for high molecular weight substrates such as growth factors far exceeds those for oxygen and glucose. An order of magnitude analysis was performed by Piret and Cooney (1991) to evaluate the relative importance of convective and diffusive contributions for oxygen transport. The radial and axial Peclet numbers were calculated for the transport of oxygen in the shell side of an Amicon P30 hollow fiber bioreactor. These authors reported a radial Peclet number of ≤ 0.02 and an axial Peclet number of ≤ 10 for the transport of oxygen in the shell space of the Amicon bioreactor.

A similar order of magnitude analysis can be carried out for glucose and the bovine serum albumin (BSA) growth factor where the diffusivity of glucose is 1×10^{-10} m^2/s and that of albumin is 7×10^{-15} m^2/s (Schonberg and Belfort, 1987; Patkar et al., 1994). Based on the parameter scales characteristic for the Amicon hollow fiber bioreactor, the radial Peclet number for glucose is ≤ 0.4 and that for albumin is ≤ 5952; while the axial Peclet number for glucose is ≤ 208 and that for albumin is $\leq 2.98\times10^{6}$. The ECS Peclet number calculations are based on a cell free shell space. Under cell filled conditions, the Peclet numbers are likely to decrease due to the resistance to flow offered by the cells.

The order of magnitude analysis serves to illustrate that the radial transport of low molecular weight solutes such as oxygen and glucose are predominantly diffusive, as indicated by low Peclet numbers in comparison to those of albumin. The radial and axial Peclet numbers of the high molecular weight substrate albumin, meanwhile, are up to five orders of magnitude greater than those of the low molecular weight counterparts. Therefore, convection is the predominant transport mechanism for high molecular weight solutes in the shell space of hollow fiber bioreactors and for this reason, convection in the ECS is a significant cause of the accumulation of these growth factors in the downstream region of the ECS. The concentration of growth factors towards the downstream section of the hollow fibers is referred to as polarization.

1.3.1.2 Experimental Perspective of Starling Flow

Protein polarization in the ECS develops due to a secondary convective flow. The circulation of fluid in the lumen introduces an axial pressure gradient which generates a secondary flow in the ECS. The nature of the secondary flow is such that luminal medium proceeds from lumen to ECS in the upstream portion of the bioreactor, while the downstream end experiences fluid flow from ECS to lumen. This may be understood in terms of fundamental fluid hydrodynamics. In the first half of the bioreactor, the pressure in the lumen exceeds that in the shell initiating fluid transport to the ECS. Meanwhile in the second half, the shell side pressure is higher than that in the lumen, leading to an equal rate of fluid exchange from the ECS to the lumen. Starling first postulated recirculation flow in capillary-tissue structures which resemble the hollow fiber bioreactor. This type of recirculation flow has since been referred to as Starling flow (Kelsey et al., 1990) and is illustrated in Figure 1.2.

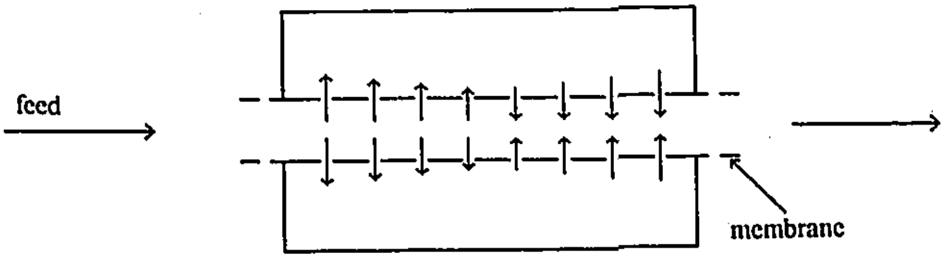

Figure 1.2. Schematic diagram illustrating Starling flow.

The flow patterns depicting Starling leakage flow in the ECS of a hollow fiber bioreactor have been experimentally verified by nuclear magnetic resonance flow imaging (Heath et al., 1990). Heath et al. (1990) performed flow measurements within the ECS of a cell free, multifiber bioreactor. The axial velocity in the ECS increased in the first half of the reactor, reaching a maximum midway along the reactor length. The axial velocity then proceeded to decrease in the second half of the reactor. Flow patterns obtained from theoretically derived velocities are in agreement with the velocity profile observed in the ECS (Heath et al., 1990; Taylor et al., 1994; Libicki et al., 1988).

During the initial inoculation of hollow fiber bioreactors, the phenomenon of protein polarization within the downstream region of the bioreactor has been observed by several researchers (Patkar et al., 1994; Piret and Cooney, 1990b; Waterland et al., 1975). Patkar et al. (1994) demonstrated the redistribution of BSA and transferrin within hollow fiber cartridges containing approximately 8000 fibers. The transient polarization of transferrin was evident following only two hours of lumen flow. At this time, the concentration profile of transferrin was such that its concentration was about 1.4 times smaller than the initial loading concentration in 75% of the upstream ECS region; in contrast, the transferrin concentration increased monotonically in the remaining quarter of the ECS region. The concentration of this same protein approximately doubled in the downstream ECS portion of the reactor. The steady state polarization of transferrin after four days of lumen fluid recirculation was also investigated by Patkar et al. (1994). A concentration profile could be described by dividing the ECS into two distinct regions: a protein free region in the upstream 95% of the ECS where Starling flow is present and a protein packed region in the downstream 5% of the ECS. This condition renders the operation of the hollow fiber bioreactor highly inefficient due to the non-uniform distribution of protein growth factors necessary in cell metabolism. In the steady-state situation, the downstream region is virtually stagnant with practically no transmembrane fluid exchange. Polarization experiments were also attempted with a solution of transferrin and albumin in the ECS. Patkar et al. (1994) observed similar concentration profiles for both proteins, for a particular BSA loading concentration.

The phenomenon of polarization is not unique to protein growth factors. The heterogeneous distribution of hybridoma cells within the ECS of ultrafiltration hollow fiber bioreactors has been detected by Piret and Cooney (1990b). The hybridoma cell culture was engaged in the synthesis of monoclonal antibody products. The ultrafiltration membrane was responsible for the retention of the antibody product in the immobilized phase. During the first month of bioreactor operation, concentration gradients in hybridoma cells resulted from the secondary convective flow in the shell space as well as the downstream polarization of high molecular weight growth factors. The concentration of cells towards the exit of the bioreactor causes diminished reactor productivities and cell numbers. Axial shell side antifibronectin antibody distributions, meanwhile, revealed accumulation of the antibody at the distal end of the hollow fiber bioreactor. In the same study, the inoculum was supplemented with the high molecular weight protein transferrin to aid in mammalian cell growth. Following eight days of lumen flow, the authors were able to correlate the downstream polarization of the transferrin growth factor with the antibody and cell distributions at the exit of the ultrafiltration reactor. Similar correlations were observed after performing the experiments for one month.

Enzyme immobilization was achieved in a hollow fiber bioreactor by Waterland et al. (1975). The axial transport and subsequent polarization of the β-galactosidase enzyme in the ECS was observed. The axial enzyme concentration profile revealed a significant axial gradient in enzyme concentration following 100 minutes of operation: the enzyme concentration at the downstream end of the reactor was reported to be twenty times greater than the upstream enzyme concentration.

1.3.1.3 Theoretical Perspective of Starling Flow

The problem of the polarization of growth factors such as BSA has been addressed from a modelling perspective by Taylor et al (1994). The model study suggests that polarization is strongly influenced by osmotically active proteins such as bovine serum albumin and transferrin. At high protein loading, the osmotic pressure of concentrated macromolecules downstream becomes large enough so that the total pressure in the ECS is capable of counteracting the hydrostatic pressure drop along the luminal length of the reactor. This observation supports the osmotic pressure model which postulates that, as the osmotic pressure of the retentate increases, permeate flux diminishes due to decreased net transmembrane pressure (Nabetani et al., 1990; Vilker et al., 1984; Wijmans et al., 1985; Wales, 1981; Shen and Probstein, 1977). Ultimately, the transmembrane fluid flux approaches zero; in essence, the bioreactor "shuts down" leaving the upstream portion depleted of protein and the downstream portion enriched with protein (Taylor et al., 1994; Patkar et al., 1994). In fact, this concentration distribution was experimentally observed by Patkar et al. (1994) during their investigation of protein distributions in hollow fiber bioreactors. The theoretical analysis put forth by Taylor et al. (1994) suggests that the downstream polarization of BSA can concentrate the protein to the extent that the solubility limit of BSA may be surpassed.

The consequences of protein polarization can be severe. Ordinarily, activities typical in the immobilized phase of a bioreactor may be divided into consumption of nutrients, accumulation of inhibitory metabolites and production of product. This perpetual cycle of consumption, accumulation and production gives rise to concentration gradients of nutrients, wastes and products. In fact, the impact of these gradients is manifested by the observation of Karel et al. (1985) who reported regions in hollow fiber reactors both deficient in cells and those containing dead cells (Schonberg and Belfort, 1987). Indeed, extreme concentrations of a nutrient can inhibit cell growth and metabolic wastes can amass to such an extent that they interfere with the natural biochemical workings of the cell (Bailey and Ollis, 1986). The production of biologically active molecules may in turn be sacrificed. Indeed, Piret et al. (1991) have also cited another consequence of nutrient and metabolite gradients: they claim that the scalability of hollow fiber bioreactors is also jeopardized when gradients are prevalent.

Convection in the ECS can lead to redistribution, or rather maldistribution, of protein or catalyst by polarizing cells or enzymes in the direction of the downstream end of the reactor. Once having reached the downstream section, the cells and catalyst may build up at the surface of the membrane. As Heath et al. (1990) have recognized, polarization of protein or catalyst will diminish optimal reactor productivity. As a consequence, substantial convective fluxes are not favoured.

1.4 Scope of the Research

Since gradients in proteins, cells and valuable products introduce heterogeneity or nonuniformity of the immobilized phase, these gradients ought to be minimized and preferably eliminated. Gradients are enhanced by convection in the ECS and are influenced by osmotically active molecules. The primary objective of this study was to assess the influence of these molecules on the hydrodynamics of hollow fiber membrane systems. This included verifying the phenomenon of concentration polarization of bovine serum albumin in a rectilinear flow cell and subsequently comparing the experimentally determined concentration profiles with those predicted by theoretical analysis. Hence, an integral part of this research involved the design and fabrication of a rectilinear flow cell. Further, it was necessary to characterize the membrane employed in the polarization experiments in addition to developing a reliable experimental protocol for HPLC analysis. Transient BSA polarization was then observed after 12, 24 and 36 hours of operation.

Complicating factors typical in hollow fiber bioreactors which are difficult to model include fiber-fiber interactions and the presence of headers at either end of the fiber. Therefore, another objective of this research was to propose a reactor design which retained the salient features of a hollow fiber reactor, yet eliminated the complicating factors. The rectilinear flow cell was designed to this end. It may be described as a rectangular two-chambered duct system with upper and lower chambers separated by a flat sheet of cellulose acetate ultrafiltration membrane which is impermeable to the macromolecule under consideration: bovine serum albumin. A protein free feed occupies the lower chamber, analogous to the lumen of a hollow fiber, while the upper chamber or extraluminal space (ELS), analogous to the ECS of a hollow fiber, contains a homogeneous solution of bovine serum albumin. As fluid from the lower chamber permeates the membrane, Starling flow is established in the upper chamber. As time progresses, convective forces in the upper chamber pack the protein towards the downstream end of the flow cell, thereby mimicking polarization in the hollow fiber bioreactor.

2. MODELLING PROTEIN POLARIZATION WITHIN A RECTILINEAR FLOW CELL

The phenomenon of protein polarization within a hollow fiber bioreactor presents a challenging biotechnological problem with serious repercussions. The task of eliminating nutrient gradients to pursue greater reactor efficiency is complicated by the presence of various factors such as Starling flow, osmotically active species and intricate bioreactor geometry. Before proposing possible solutions to HFBR polarization, a thorough understanding of the contributions of these complicating factors is required. A study of the effects of several variables on hollow fiber bioreactor hydrodynamics is further facilitated by a mathematical model of the system. The mathematical model in this research simulates albumin polarization prevalent in the extraluminal space of a rectangular flow cell. It is based on the hollow fiber membrane model by Taylor et al. (1994) and was furnished by Dr. Taylor for this project, along with a FORTRAN program to simulate the transient polarization of osmotically active solutes within the upper chamber of a rectangular flow cell.

The construction of the mathematical model may be viewed as a two-stage endeavor. The first stage consists of accurately describing the physical situation, that is, polarization of protein, with appropriate theoretical equations. For the problem at hand, this involves the incorporation of mass and momentum balances as well as membrane transport equations and an osmotic pressure relationship. The model involves descriptions of the coupled processes of fluid flow within the cell and the transient redistribution of protein within the extraluminal space. The second stage of modelling consists of developing an appropriate solution technique; in this case, a numerical procedure. These two aspects of the model will be discussed in the following sections.

2.1 Theoretical Considerations

2.1.1 Lumen and ELS Hydrodynamics

The following analysis is based on the models of Taylor et al. (1994) and Patkar et al. (1994) and modified to accommodate the rectilinear geometry of the flow cell. The reader is referred to the previous modelling work for details. The rectilinear flow cell used to conduct protein polarization experiments may be described as a two-chambered duct system. The upper chamber is similar to the ECS of a hollow fiber bioreactor and the lower chamber is analogous to the lumen. These two chambers are separated by an ultrafiltration membrane intended to retain the albumin within the upper chamber. The polarization of BSA in the downstream section of the upper chamber is expected during the recirculation of a protein free feed in the lower chamber. Figure 2.1 illustrates a schematic diagram of the rectilinear flow cell.

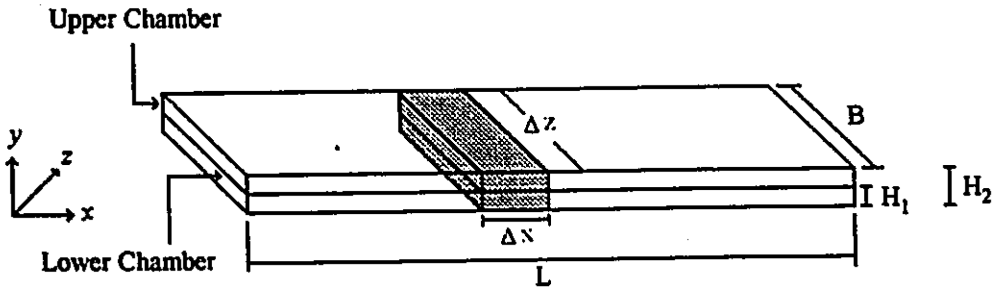

Figure 2.1. Schematic diagram of the rectilinear flow cell used for polarization experiments.

Assuming that the total rate of fluid exchange between the upper and lower chambers of the flow cell is small compared to the total fluid flow rate through the system, the local fluid velocities within each chamber may be described by the fully developed

Poiseuille flow through a rectangular duct. A one-dimensional mathematical model which neglects gradients in the transverse direction is used. In this case, assuming flow occurs in the x-direction, the continuity and momentum equations in Cartesian coordinates simplify to that for duct flow. It should be noted that this approximation is not valid at the entrance and the exit where transverse pressure gradients and fluid velocities become significant. However, this represents only a minor portion of the entire system (Taylor et al., 1994) and is ignored here.

When the velocity distribution is integrated over the cross sectional area of the duct, the relation for the volumetric flow rate is found to be (White, 1991)

$$Q_L = \frac{4}{3}\frac{b a^3}{\mu}\left(-\frac{dP_L}{dx}\right)\left[1 - \frac{192a}{\pi^5}\sum_{i=1,3,5,\ldots}^{\infty}\frac{\tanh(i\pi b/2a)}{i^5}\right], \qquad (2.1)$$

where Q_L refers to the volumetric flow rate in the lumen, a is one half the width of the rectangular duct and b is one half its height. The average fluid velocity in the x direction becomes (White, 1991)

$$\bar{u}_L = \frac{Q_L}{4ba} = \frac{a^2}{3\mu}\left(-\frac{dP_L}{dx}\right)\left[1 - \frac{192a}{\pi^5 b}\sum_{i=1,3,5,\ldots}^{\infty}\frac{\tanh(i\pi b/2a)}{i^5}\right]. \qquad (2.2)$$

Equation (2.2) can be rearranged to accommodate the specific geometry of the flow cell under consideration by introducing pertinent physical dimensions such as width of cell, B, and height of lower chamber, H_1, defined by

$$2a = B, \qquad (2.3a)$$

$$2b = H_1. \qquad (2.3b)$$

The average flow velocity in terms of H_1 and B is

$$\bar{u}_L = \frac{B^2}{12\mu}\left(-\frac{dP_L}{dx}\right)\left[1-\frac{192B}{\pi^5 H_1}\sum_{i=1,3,5...}^{\infty}\frac{\tanh(i\pi H_1/2B)}{i^5}\right]. \qquad (2.4)$$

A similar expression for the average flow velocity in the upper chamber results when the upper chamber height, ΔH is substituted for H_1 in Eq. (2.4)

$$\bar{u}_E = \frac{B^2}{12\mu}\left(-\frac{dP_E}{dx}\right)\left[1-\frac{192B}{\pi^5 \Delta H}\sum_{i=1,3,5...}^{\infty}\frac{\tanh(i\pi \Delta H/2B)}{i^5}\right]. \qquad (2.5)$$

Again, it is assumed here that the local rate of fluid exchange across the membrane is small relative to the local flowrate within the upper chamber. The magnitude of ΔH is easily obtained from the following relation and is also indicated in Figure 2.1

$$\Delta H = H_2 - H_1. \qquad (2.6)$$

2.1.2 Membrane Hydrodynamics

The transmembrane flux from lower to upper chamber may be expressed in terms of the hydrostatic pressure in both chambers as well as the colloid osmotic pressure exerted in the ELS. Darcy's law is invoked when considering flow within the membrane and is justified here since we have low Reynolds number flow of an incompressible Newtonian fluid through a porous membrane. The differential form of Darcy's Law, assuming the membrane is isotropic and homogeneous, is

$$V_M = -\left(\frac{k}{\mu}\right)\left[\frac{\partial P_M}{\partial x}+\frac{\partial P_M}{\partial y}+\frac{\partial P_M}{\partial z}\right]. \qquad (2.7)$$

In the above equation, V_M is the membrane superficial velocity, k is the Darcy permeability, μ is the fluid viscosity and P_M is the pressure within the membrane structure. Fluid flow within the membrane is also governed by the continuity equation

$$\frac{\partial V_M}{\partial x}+\frac{\partial V_M}{\partial y}+\frac{\partial V_M}{\partial z}=0. \tag{2.8}$$

Substituting Eq. (2.7) into Eq. (2.8) then yields

$$-\left(\frac{k}{\mu}\right)\left[\frac{\partial^2 P_M}{\partial x^2}+\frac{\partial^2 P_M}{\partial y^2}+\frac{\partial^2 P_M}{\partial z^2}\right]=0. \tag{2.9}$$

The longitudinal pressure gradients in the lumen and ELS are negligible compared to the transverse gradients through the membrane. This arises due to the exceedingly low aspect ratios, $\Delta H/L$ and H_1/L, characteristic of upper and lower chambers of the flow cell, respectively, and the extremely high hydraulic resistance (low conductivity) typical of the ultrafiltration membrane in the flow cell. Hence, Eq. (2.7) can be simplified to include only the transverse pressure term:

$$V_M=-\frac{k}{\mu}\frac{dP_M}{dy}. \tag{2.10}$$

The solution of the second order ordinary differential equation demands two constraints in the form of two boundary conditions relating P_M to the hydrostatic pressure in the upper and lower chambers, P_E and P_L respectively, and the protein osmotic pressure, Π_E, in the ELS:

$$P_M = P_L(x) \quad \text{at} \quad y = H_1. \tag{2.11a}$$

$$P_M = P_E(x) - \Pi_E \quad \text{at} \quad y = H. \tag{2.11b}$$

The height H refers to the lower chamber height plus the membrane thickness. The final membrane pressure distribution then takes the form

$$P_M = P_L + \frac{P_L - (P_E - \Pi_E)}{H_1 - H}(y - H_1). \tag{2.12}$$

Substituting Eq. (2.12) into Darcy's Law yields the desired expression relating the transmembrane fluid flux from lower to upper chamber to the relevant pressures

$$V_M = -\frac{k}{\mu(H_1 - H)}\left[P_L - P_E + \Pi_E\right]. \tag{2.13}$$

The quantity $-k/(H_1-H)$ can be replaced by L_P, the membrane permeability to yield

$$V_M = \frac{L_P}{\mu}\left[P_L - P_E + \Pi_E\right]. \tag{2.14}$$

2.1.3 Overall and Differential Fluid Balances

Consider a differential segment of the lower chamber, as illustrated in Figure 2.1. A material balance over a stationary volume element $\Delta x \Delta y \Delta z$ is achieved by equating inlet and outlet volumetric flow rates leading to the following relationship:

$$H_1 \frac{d\bar{u}_L}{dx} = -V_M. \tag{2.15}$$

where V_M is the transmembrane flux from lower to upper chamber. Substituting Eq.

(2.14) into Eq. (2.15) provides an expression for the velocity gradient in the lumen in terms of the relevant pressure forces:

$$\frac{d\bar{u}_L}{dx} = -\frac{L_p}{\mu H_l}\left[P_L - P_E + \Pi_E\right]. \qquad (2.16)$$

Differentiating Eq. (2.16) with respect to x gives

$$\frac{d^2\bar{u}_L}{dx^2} = -\frac{L_p}{\mu H_l}\left[\frac{dP_L}{dx} - \frac{dP_E}{dx} + \frac{d\Pi_E}{dx}\right], \qquad (2.17)$$

which provides a second-order differential equation relating $\bar{u}_L$ to P_L, P_E and Π_E. To relate the average velocity in the upper chamber, $\bar{u}_E$, to its counterpart in the lower chamber, $\bar{u}_L$, an overall mass balance on the fluid within the system is necessary. The appropriate schematic representation with pertinent terms is shown in Figure 2.2.

Figure 2.2. Schematic diagram illustrating an overall mass balance on the fluid within the flow cell.

The desired expression is furnished by equating inlet and outlet volumetric flow rates associated with the membrane segment:

$$\bar{u}_E(x) = \frac{H_l}{\Delta H}\left[\bar{u}_{L0} - \bar{u}_L(x)\right]. \qquad (2.18)$$

In the above equation, $\bar{u}_E(x)$ is the local fluid velocity at some point x in the ELS, $\bar{u}_L(x)$ is the local fluid velocity in the lumen at that point and $\bar{u}_{Lo}$ is the inlet luminal velocity.

At this point, several useful relationships have been established which can now serve to redefine the flow field in the lower chamber. The pressure gradients in the lumen and ELS may be isolated from Eqs. (2.4) and (2.5), respectively. Substitution of these pressure gradient expressions and Eq. (2.18) into Eq. (2.17) generates the equation of interest

$$\frac{d^2\bar{u}_L}{dx^2}=\frac{L_p}{\mu H_l}\left[m_L\bar{u}_L-m_E\left(\bar{u}_{Lo}-\bar{u}_L\right)-\frac{d\Pi_E}{dx}\right], \tag{2.19}$$

where m_L and m_E are given by

$$m_L=\frac{12\mu}{B^2}\frac{1}{1-\frac{192B}{\pi^5 H_l}\sum\limits_{i=1,3,5,\ldots}^{\infty}\frac{\tanh(i\pi H_l/2B)}{i^5}}; \tag{2.20}$$

$$m_E=\frac{12\mu H_l}{B^2\Delta H}\frac{1}{1-\frac{192B}{\pi^5\Delta H}\sum\limits_{i=1,3,5,\ldots}^{\infty}\frac{\tanh(i\pi\Delta H/2B)}{i^5}}. \tag{2.21}$$

Equation (2.19) provides a final equation relating the average local fluid velocity in the lower chamber to the various components which contribute to the flow field there, such as the osmotic pressure of solute in the ELS, the inlet and outlet lumen velocity, the geometric dimensions of the flow cell and the membrane conductivity.

2.1.4 Protein Osmotic, Lumen and ELS Pressures

The solution of the flow field requires knowledge of the osmotic pressure, Π_E. This is provided by Patkar et al. (1994) in the form of a virial equation which relates osmotic pressure and albumin concentration:

$$\Pi_E = \frac{C_E RT}{M_P}(1 + A_1 C_E + A_2 C_E^2), \tag{2.22}$$

where M_P is the molecular weight of protein, C_E is albumin concentration, R is the universal gas constant and T is the absolute temperature. Meanwhile, the coefficients of the second and third terms of the virial expansion, A_1 and A_2, are 10.473×10^{-3} m^3/kg and 17.374×10^{-6} m^3/kg, respectively (Patkar et al., 1994). Differentiating Eq. (2.22) with respect to x renders one term of Eq. (2.19)

$$\frac{d\Pi_E}{dx} = \frac{RT}{M_P}(1 + 2A_1 C_E + 3A_2 C_E^2)\frac{dC_E}{dx}. \tag{2.23}$$

In addition to the osmotic pressure, the luminal and extraluminal pressure distributions are also of interest. Rearranging Eq. (2.4) and integrating leads to the following expression for the pressure distribution in the lumen:

$$-\int_{P_0}^{P} dP_L = \int_0^x \bar{u}_L \frac{12\mu}{B^2} \frac{1}{1 - \frac{192B}{\pi^5 H_1}\sum\limits_{i=1,3,5,\ldots}^{\infty} \frac{\tanh\,(i\pi H_1/2B)}{i^5}}\,dx. \tag{2.24}$$

The pressure distribution in the ELS, P_E, is obtained from the transmembrane flux expression given by Eq. (2.14).

2.1.5 Protein Transport within the Upper Chamber

The transient distribution of protein in the extraluminal space is governed by the convection-diffusion equation:

$$-\frac{\partial C_E}{\partial t} = \frac{\partial}{\partial x}\left(uC_E - D\frac{\partial C_E}{\partial x}\right), \tag{2.25}$$

where D is the diffusion coefficient of the protein. Equation (2.25) represents a solute mass balance and applies in the absence of any sinks or sources. The relevant boundary conditions reflect the physical constraint that no exchange of protein across the boundaries of the ELS is possible, including the membrane. The following boundary conditions therefore apply:

$$C_{EO} = C_E \text{ at } 0 \leq x \leq L,\ t = 0 \tag{2.26a}$$

$$\frac{\partial C_E}{\partial z} = 0 \text{ at } x = 0,\ t \geq 0 \tag{2.26b}$$

$$\frac{\partial C_E}{\partial z} = 0 \text{ at } x = L,\ t \geq 0. \tag{2.26c}$$

The last boundary condition states that protein convection and diffusion are equal and opposite at the membrane surface (Taylor et al., 1994).

2.2 Numerical Techniques

Discretization methods permit the governing differential equations to be replaced with simple, algebraic equations suitable for numerical solution (Patankar, 1981). The discretization equations in this study are derived from a power-law formulation developed by Patankar (1981). The governing equations defining the dependent variables such as velocity, concentration and pressure are discretized within the flow cell reactor. The essence of the numerical simulation consists of updating the luminal velocity field at each time step until a converged concentration profile in the ELS has emerged. The steady state concentration profile is achieved only when the protein concentration remains invariant with respect to time. In the interim, transient protein polarization may be investigated.

A typical iteration starts with assigning an initial protein concentration, equal to the value from the previous time step, at each node throughout the ELS. The gradient in osmotic pressure is calculated from

$$\frac{d\Pi_E}{dx} = \frac{d\Pi_E}{dC_E}\frac{dC_E}{dx}, \tag{2.27}$$

where $d\Pi_E/dC_E$ is known from Patkar's relation given by Eq. (2.23) and dC_E/dx is generated by a cubic spline fit of the concentration distribution within the ELS at each nodal point. Fortunately, inherent to the cubic spline fit is the assessment of the derivative of ELS concentration at each point. Knowledge of both the ELS concentration and its derivative allows determination of $d\Pi/dx$, according to Eq. (2.23).

The luminal flow field described by the second order ordinary differential, Eq. (2.4), is a linear differential equation and can be solved using the linear shooting method as outlined by Burden et al. (1981) to yield $\bar{u}_L$. The linear shooting algorithm consists of replacing the original boundary-value problem with two initial-value problems. The final solution of the luminal velocity distribution is a linear combination of the solutions to the two initial-value problems. One part of the solution for $\bar{u}_L$ is solved analytically while the other part of the solution is solved numerically. The numerical portion of the solution for $\bar{u}_L$ is solved using a fourth order Runge-Kutta algorithm. The shell side velocity, meanwhile, is related to the luminal velocity flow field as demonstrated by Eq. (2.18).

The newly acquired shell side velocity is used to calculate a revised shell side concentration. The solute distribution in the ELS is determined by applying Patankar's discretization procedure along with the power law scheme. The discretization equations at this stage are devised for the shell side concentration and derived from the solute and fluid continuity equations. The Thomas algorithm is used to solve the algebraic discretization equations, yielding the concentration profile of bovine serum albumin in the ELS. The most recent values of the shell side concentrations are compared to those initially specified. If the magnitude of the difference between the current and previous ELS concentrations, denoted as ΔC_E, does not meet the required tolerance as specified by Eq. (2.28) below, the next priority becomes to update the luminal velocity field using the prevailing concentration in the subsequent iteration. The quantity C_E^{max} in Eq. (2.28) refers to the maximum value of $C_E(x)$ for a given iteration.

$$\frac{\Delta C_E}{C_E^{max}} \leq \text{tol.} \tag{2.28}$$

Hence, another iteration is initiated whereby the ELS concentrations are fitted to a cubic spline and both the luminal and ELS flow fields are computed anew. The iterations are continued until convergence is successful or the maximum number of iterations has been exceeded.

The numerical simulation also calculates the luminal and ELS pressures at each nodal point. The luminal pressure distribution is determined by first fitting the luminal velocity to a cubic spline within each nodal interval. The resulting cubic polynomial is integrated analytically to obtain the luminal pressure distribution, in accordance with Eq. (2.24). The ELS pressure distribution at each nodal point is evaluated from Eq. (2.14). The osmotic pressure, meanwhile, is determined from the nodal value of C_E using Eq. (2.22). The total pressure in the upper chamber is then given by the difference between the ELS hydrostatic and osmotic pressures.

3. EXPERIMENTAL DESIGN AND METHODOLOGY

3.1 Design of The Rectilinear Flow Cell

3.1.1 Design Considerations

In this research, isolation of the effect of osmotically active BSA on the hydrodynamics of a membrane bioreactor was pursued. Hence, one of the main objectives of the research was the design and construction of the membrane flow cell used to conduct protein polarization experiments. A design was proposed following a study of existing membrane bioreactor configurations. From a design perspective, it was particularly worthwhile to focus on possible complicating factors typical in hollow fiber membrane bioreactors such as fiber-fiber interactions, methods of sampling and the header design. The consequences of some of these factors would have proved difficult to model and a comparison of simulated results with experimental ones would have been questionable. Therefore, a study of potential design complications was warranted as the first stage of flow cell design.

Fiber-fiber interactions represented one complicating factor in a typical hollow fiber bioreactor. These bioreactors consist of a bundle of hundreds or thousands of fibers. Buoyancy effects may promote crossflow between neighbouring fibers, illustrating an instance of fiber-fiber interactions (Taylor et al., 1994). Interactions between component fibers are inevitable and therefore may need to be accounted for when modeling protein polarization in such a reactor. A practical method for sampling from the bioreactor was also an important design concern. For example, Piret and Cooney (1990b) determined cell distributions in the shell side space of a hollow fiber cartridge by freezing and sectioning the cartridge. This method of sampling the shell side space entailed sacrificing the hollow fiber cartridge at the termination of each experiment. Waterland et al. (1975) also observed this procedure of sacrificing hollow fiber cartridges while studying the shell side polarization of β-galactosidase. This was a rather costly means of obtaining samples. Thirdly, the headers used in hollow fiber cartridges are not necessarily optimized to maintain uniform flow and may result in uneven flow distribution and subsequent fiber-fiber interactions.

The ideal flow cell design would minimize or preferably eliminate these complicating factors while retaining the salient features of the hollow fiber bioreactor. The cell design also had to be amenable to sampling. For reasons given above, a rectilinear geometry was adopted which was intended to simulate the basic functional unit of a hollow fiber bioreactor, that is, a single hollow fiber membrane and its local extra-luminal space. The basic structure of the flow cell consisted of a two chambered duct system, where each chamber was a rectangular channel. The lower chamber was analogous to the luminal space of a hollow fiber while the upper chamber simulated its extracapillary space. Both chambers were separated by a flat sheet membrane. Since only a single fiber was modelled by the flow cell, headers were not required in the design. A schematic diagram of the rectilinear flow cell used in the polarization experiments is shown in Figure 3.1.

3.1.2 Design Constraints

The first design criterion addressed was the selection of flow cell dimensions, namely the chamber length, chamber width, lower chamber height, and total chamber height, where the total chamber height referred to the combined heights of the upper and lower chambers. The decision to deem particular dimensions acceptable was aided by imposing certain constraints as well as adhering to practical limitations associated with the construction of the flow cell. A constraint proving useful in this regard was the restriction that only those dimensions which favored comparatively rapid polarization of BSA would

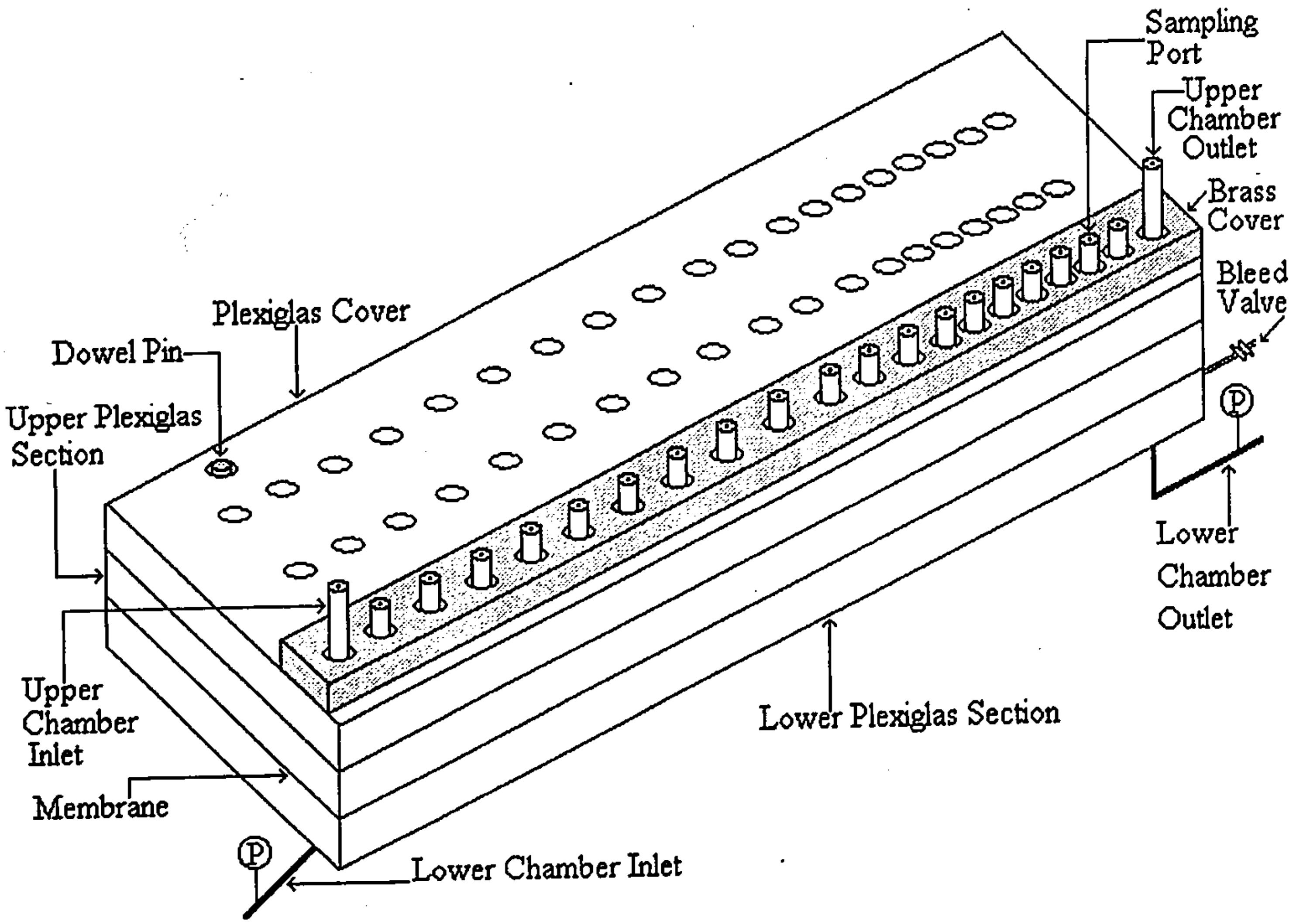

Figure 3.1. Schematic diagram of the rectilinear flow cell.

be considered; an acceptable period of time was arbitrarily chosen to be on the order of a few days.

Another constraint to contend with in the selection of flow cell dimensions was the requirement that the total volume of sampling represent a negligible fraction of the total upper chamber fluid volume, since large sample volumes could lead to fluid mixing between adjacent sampling ports. In the original flow cell design, a sampling volume not exceeding 2% of the upper chamber volume was set. Therefore, flow cell dimensions had to be chosen to accommodate an appropriate upper chamber volume. However, due to experimental limitations with the HPLC system, the actual sampling volume was approximately 7%.

An additional limitation which served to narrow the alternatives available for assigning reactor dimensions was the issue of stretching the membrane between the upper and lower chambers. For the purpose of the current research, it was necessary to maintain the membrane taut and even throughout the entire chamber length. Intermittent sagging of the membrane was undesirable since it affected the exposed surface areas of both the upper and lower chambers. The uncertainty in chamber area associated with membrane distortion may have led to a discrepancy between experimental and numerical predictions of BSA concentrations. The maintenance of a taut membrane was facilitated by assigning a narrow chamber, in contrast to a broad one.

A practical restriction associated with the construction of the flow cell which also assisted in the choice of flow cell dimensions was the inherent limitation of the milling saw tool available to set the cell length. The milling saw in the machine shop of the Chemical Engineering Department was only capable of cutting to maximum length of 0.6 m (60 cm), which served as an upper limit for the length of the rectangular flow cell.

Another practical limitation recognized in the early stages of flow cell design pertained to the material of construction of the cell. At the onset, two possibilities existed: stainless steel and Plexiglas. Stainless steel was an attractive option due to its resistance to corrosion. However, construction of a stainless steel flow cell within specified precision represented a time consuming and expensive undertaking. Plexiglas, on the other hand, afforded the advantages of short construction time as well as reasonable expense. Further, due to the innocuous and inert nature of the solvents used in this research, the susceptibility of Plexiglas to reaction with these solvents was considered negligible and so it was chosen over stainless steel.

The design of the rectangular flow cell began with establishing cell dimensions and, to this end, the constraints presented thus far aided in their selection. The stipulation that polarization of BSA occur within a short time period for a given set of cell dimensions required estimates of the transient concentration distribution prior to the commencement of experiments. At this stage, the numerical model was exploited for its prediction of BSA concentration profiles as a function of various geometric factors and operating conditions such as the average fluid velocity in the lower chamber, initial protein loading, and membrane permeability. In this manner, the numerical model provided by Taylor et al. (1994) was an extremely useful design tool.

In particular, the effects of seven variables on flow cell performance were studied, including chamber length, chamber width, lower chamber height, total chamber height, average fluid velocity in the lower chamber, initial protein loading concentration and membrane permeability. A simplified fractional factorial design was used to elucidate the effect of each variable on protein distribution in the upper chamber, whereby only the individual effect of each variable was investigated. In other words, a complete factorial design may have yielded extreme protein polarization at parameter set points different than those examined in the fractional factorial design where only one variable was changed at a time. However, the objective of this design effort was not one of cell optimization but rather one of illustrating the transient polarization of BSA within a reasonable period of time. Therefore, in order to satisfy this objective, it was sufficient to examine only first order interactions.

Each of the seven variables of interest assumed three possible values. The operating range of each variable was selected so as to simulate the operating conditions of a hollow fiber bioreactor. For example, a typical hollow fiber exhibits a length which is several hundred times its radius. In an attempt to simulate such a hollow fiber, the geometric variables were tested at the following three conditions: chamber length: 0.1, 0.3, 1 m; chamber width: 0.002, 0.005, 0.01 m; lower chamber height: 0.001, 0.005, 0.01 m; total chamber height: 0.006, 0.01, 0.015 m. An appropriate range of values to assign the inlet lumen velocity, initial albumin loading concentration and membrane permeability emerged from a model study conducted by Taylor et al. (1994) on BSA polarization in isotropic membrane hollow fiber bioreactors. For example, a membrane conductivity on the order of 10^{-10} m^2s/kg was used in that study. The membrane conductivity in the numerical model was also tested at an order of magnitude larger and smaller than this. The initial protein loading concentrations employed by Taylor and coworkers were 1, 10, 25, 50 and 100 kg/m^3, while those specified in the numerical simulation were 10, 100 and 1000 kg/m^3. The inlet lumen velocity used in the model study was 0.05 m/s, while initial flow cell design simulations were performed at 0.01, 0.1 and 0.25 m/s.

The results of the numerical simulations were analyzed by plotting BSA concentration as a function of longitudinal distance along the cell length at various times during the simulation. The results indicated that a longer flow cell length favoured greater albumin polarization for a given time duration. Likewise, a smaller chamber width, lower chamber height and total chamber height each promoted significant protein polarization. The numerical simulations also confirmed that a higher inlet lumen velocity and membrane conductivity each contributed to a greater degree of polarization. A lower initial protein loading concentration led to a more dramatic polarization than higher initial loading concentrations.

The recommended flow cell design thus consisted of long, narrow and shallow chambers. The smallest dimension of chamber width, lower chamber height and total chamber height which could be machined with reasonable accuracy was 0.0025 m. The limitation of the milling saw, meanwhile, imposed a maximum chamber length of 0.6 m. Each of the upper and lower chambers was machined within a 0.0191 m (3/4 inch) thick slab of Plexiglas. The finalized dimensions of the flow cell were input into the numerical model to verify that the desired transient polarizations were indeed observed. Further simulations investigating the effects of inlet lumen velocity, initial protein loading concentration and membrane conductivity were then carried out to identify suitable experimental test conditions.

Once the dimensions of the rectangular flow cell were decided, the next aspect of the design challenge which needed to be considered was the issue of sampling. There were several difficulties associated with sampling fluid from the upper chamber. First of all, the sampling syringe had to be inserted into the upper chamber without puncturing the membrane sheet below. This was assured by equipping each sampling port with a guide to direct the syringe to an appropriate depth within the upper chamber. The syringe guides incorporated into the flow cell design consisted of glass capillary tubes, 0.05 m long. The sampling syringe was inserted in the orifice forming the internal diameter of the capillary tube. In addition to serving as guides, the capillary tubes provided structural support for the syringes.

Protein leakage from the upper chamber was avoided by the use of gas tight rubber septa. These septa were placed at the base of the capillary guides and functioned well to seal the openings holding the capillaries, as well as to seal the punctures created by insertion of syringes. The combination of capillary tube and gas tight septum formed a sample port. Sample ports were placed along the length of the flow cell.

According to the numerical simulations, the total pressure prevalent in the upper chamber was on the order of 30 000 Pa. If the capillary tubes are subjected to such a pressure, they risk being displaced from the openings which contain them and so needed to be secured in place. During the design stage of the flow cell, an upper limit of 34475 Pa

(5 psi) was imposed as the maximum pressure sustainable by the capillary tubes. Gluing the capillary tube to either the septum immediately below or to the bore in the Plexiglas surrounding the glass tube was not practical since, in the event where the septum had to be replaced, the glued capillary tube would have been difficult to remove. Thus, the design difficulty lay with accommodating two goals at once: allowing for easy removal of the capillary tubes yet being able to secure the tubes so that they were not loose and vulnerable to popping. By way of solution, two plastic set screws, one on either side of the capillary tube, were used to secure the glass tubes, enabling them to resist being displaced under a pressure of 34475 Pa (5 psi) while at the same time providing a simple means of removing the capillary tubes from the cell, if necessary.

Estimates of BSA concentration profiles through numerical simulations at the initial design stage aided in selecting the precise locations of the sampling ports along the length of the flow cell. Significant polarization of protein was expected to occur at the downstream end of the cell, leaving a virtually protein free region in the upstream section in some cases. For this reason the sample ports were concentrated somewhat in the downstream portion of the cell. In fact, three distinct distances were chosen between sample ports over the length of the 0.6 m long flow cell. The first ten sampling ports were 0.0456 m apart. The following three ports were located 0.023 m apart and the last six sampling ports were spaced 0.015 m apart. The comparatively large number of sampling ports allowed for flexibility in selecting sample sites between individual experiments.

The upper section of Plexiglas was fitted with two glass capillary tubes, one at the inlet of the upper channel and one at the outlet, which served as inlet and outlet ports during filling of the upper chamber. These capillary tubes were constructed similar to the sampling ports and were furnished with gas tight septa at their base. Fluid could be pumped into or out of the upper chamber by inserting a thin syringe into either inlet or outlet capillary tube and penetrating the septum below. In contrast, filling and emptying of the lower chamber was achieved by constructing two openings at the inlet and outlet of the lower chamber.

To assure consistent assemblage of the flow cell, two dowel pins were used to align the upper section of Plexiglas with the lower section. Once the pins were positioned in the lower section, it became a trivial matter to slide the upper section of Plexiglas onto the pins.

3.1.3 Assembly of the Rectilinear Flow Cell

At this point, the dimensions of the flow cell were known and a sampling method had been proposed. The next critical design concern pertained to the assembly of the flow cell without developing leaks. In particular, the flow cell had to be able to withstand several successive experiments, each lasting a few days, without the occurrence of leaks. A considerable amount of time was devoted to discovering a suitable technique.

It was evident that a gasket was necessary around the upper and lower chambers to prevent fluid spillage from these sections. Initially, silicon grease was applied along the contours of the upper and lower chambers. A strip of membrane wider than the width of either chamber was placed between the two chambers. A slab of 0.0191 m (3/4 inch) Plexiglas was then fitted on top of the cell to provide the extra weight to maintain the membrane taut and even. Several C-clamps were also used on both sides of the cell in order to squeeze the Plexiglas cover down and distribute its weight evenly along the length of the cell. Circulation of water in the lower chamber was initiated immediately after fastening the C-clamps. In this manner, water could permeate through the membrane and into the upper chamber. Unfortunately, leakage of water was observed shortly thereafter, suggesting that silicon grease was inadequate to prevent leaks. Several other trials incorporating combinations of silicon grease, Beckman grease, double sided tape and C-clamps were unsuccessful. At this stage, the problem of leaking was attributed, in part, to an uneven and weak pressure distribution along the length of the flow cell. It was believed that the weight of the Plexiglas was insufficient to maintain the membrane taut and even. If the membrane was not completely flat while residing between the upper and lower chambers, leakage of chamber fluids was inevitable. The solution lay in mounting a heavier piece consisting of a brass strip 0.6 m long and 0.01 m high on top of the Plexiglas cover. Openings for sample ports were drilled into the strip of brass, allowing it to fit easily over the Plexiglas. The brass piece was cut to a width of 0.05 m so that it would not hinder viewing the channel below. Once the brass piece was mounted on top of the cell, the presence or absence of leaks could be determined by looking down on either side of the brass weight, through the Plexiglas.

The following methodology for assembling the flow cell without the threat of leaks proved successful. Prior to actually assembling the cell, the surfaces of Plexiglas were cleaned and smoothed. Care was taken to avoid scratching the Plexiglas surface, since these scratches could serve as tiny channels through which fluid can leak. Next, double sided tape was cut to a width of 0.015 m and placed along the perimeter of the upper and lower channels, thereby serving as a gasket for the system. Silicon glue was then applied on the outer edges of the tape around the chamber grooves using a fine brush. It was important to restrict the glue to the outer edges of the tape, otherwise the silicone glue could penetrate into the groove when the clamps were tightened to the cell.

Following the application of silicone glue a strip of membrane 0.57 m long and 0.015 m wide was centered over the upper channel, allowing it to comfortably cover the chamber groove which was 0.0025 m wide. The polymer side of the membrane was to be in contact with the protein solution. The silicone glue was subsequently applied over that portion of the membrane backing which was not directly over the groove. Care was taken to ensure that the silicone glue was not applied over the groove, to avoid blocking the membrane. The upper and lower chambers were now ready to be fitted together. The two dowel pins were positioned diagonally across from one another in the lower section of Plexiglas and the upper chamber slid into place, resulting in a two chambered duct system with each chamber separated by a flat sheet membrane. At this point, the Plexiglas cover was placed on top of the cell, followed by the brass strip. A total of thirteen C-clamps were then fastened along the side of the cell to firmly press three layers of 0.0191 m (3/4 inch) thick Plexiglas along with a 0.0127 m (1/2 inch) thick brass strip together. After completing assembly of the flow cell, the silicone glue was permitted to dry for at least 6 hours. It was important, however, not to let the glue dry for too long otherwise the membrane in the cell could run dry. Circulation of fluid in the upper and lower chambers could then begin.

After the first prototype of the flow cell was built, the occurrence of an air pocket at the outlet of the lower chamber was obvious. Therefore, a bleed valve was introduced directly into the air pocket and proved to be effective at removing the air from the lower chamber.

A final design modification centered around disassembling the flow cell, which was difficult due to the double sided tape and silicone glue. A rather innovative method for disassembling the flow cell was subsequently developed. Three holes were drilled through the upper section of Plexiglas in close proximity to the upper chamber. These three holes allowed three threaded screws, each approximately 0.06 m long, to be screwed into the upper section of Plexiglas. As the screws were tightened, they penetrated the upper section of Plexiglas until they eventually touched the top of the lower slab of Plexiglas. Further tightening with a wrench resulted in the prying apart of the upper section of Plexiglas from the lower one.

3.2 Membrane Characterization

A flat sheet, cellulose acetate, ultrafiltration membrane with a molecular weight cut off of 1-5 kDa, as reported by the Osmonics manufacturer, was used in this research to immobilize BSA within the upper chamber of the flow cell. Although the cellulose acetate membrane was supposed to be homogeneous and isotropic, local variations in the permeability were inevitable during its production. Therefore, the magnitude of the membrane permeability was experimentally determined at various locations throughout the membrane sheet. It was important to obtain as accurate a value for the membrane permeability as possible, since this quantity would consequently be used in the numerical simulations to compare model predictions of the BSA concentration profiles to those determined experimentally, and since it strongly influenced the predicted profiles.

The experimental procedure for determining the membrane permeability will now be presented. The cellulose acetate membrane was stored in a solution of 0.5 % v/v formaldehyde according to the manufacturer's directions. Six circular membrane sections or coupons, each approximately 0.05 m (5 cm) in diameter, were cut from the total cross section of the flat sheet. The coupons were concentrated in the region of the membrane where strips would later be obtained for implementation in the flow cell. The locations of the cellulose acetate coupons are illustrated in Figure 3.2. These locations were selected to test for uniformity of membrane permeability in the vertical, horizontal and diagonal directions.

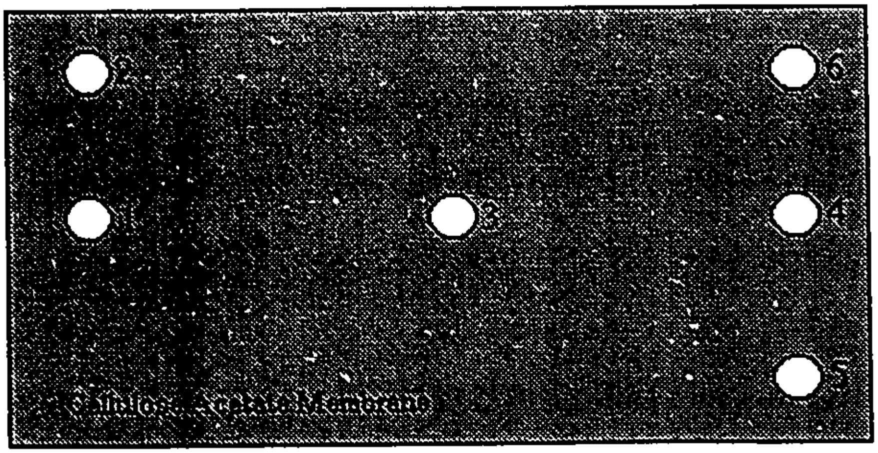

Figure 3.2. Schematic diagram illustrating locations of six membrane coupons used for the determination of membrane permeability of the flat sheet, cellulose acetate membrane.

The coupons were cut 0.05 m (5 cm) in diameter, enabling them to fit in circular test cells. Each test cell consisted of a feed side and a permeate side. A single coupon was inserted into one test cell with the polymer coated side of the membrane in contact with the retentate side of the test cell. This procedure was repeated for the two other cells. A torque wrench was used to tighten the cells and apply the same force to each coupon, thereby assuring that the area of membrane available for permeation was the same in all cases. The reason for this was the presence of a rubber O-ring surrounding the circular membrane coupon which could flatten and reduce the exposed area of membrane when the cell was tightened. The three test cells were arranged in series, as indicated by a schematic diagram of the membrane characterization apparatus in Figure 3.3, to expedite the characterization process.

A calibrated precision pressure gauge was placed at the outlet of the third test cell, while a pressure transducer was positioned at the inlet to the first test cell. The pressure gauge and the transducer were used to compute the overall pressure drop across all three test cells. The membrane characterization experiments began with the determination of the permeability of the membrane coupons to deionized water. For these experiments, deionized 18 MΩ water was obtained from a Milli-Q system. The deaeration of deionized water, which was necessary to avoid air bubbles in the test cells, was accomplished by placing the reservoir of water on a magnetic stirring plate and attaching the reservoir to a vacuum pump. Deaeration proceeded for 15 minutes. The water was then pumped to the inlet feed of the first test cell and recirculated back to the reservoir through the outlet of the third cell, as shown in Figure 3.3.

Initially, deionized water was recirculated through all three test cells for 24 hours to condition the surfaces of the membrane coupons. The outlet pressure was controlled by a valve, demonstrated in Figure 3.3. Following the conditioning procedure, permeation rates of water through the membrane coupons, as a function of overall pressure drop, were recorded. Each experiment consisted of first setting the outlet pressure by

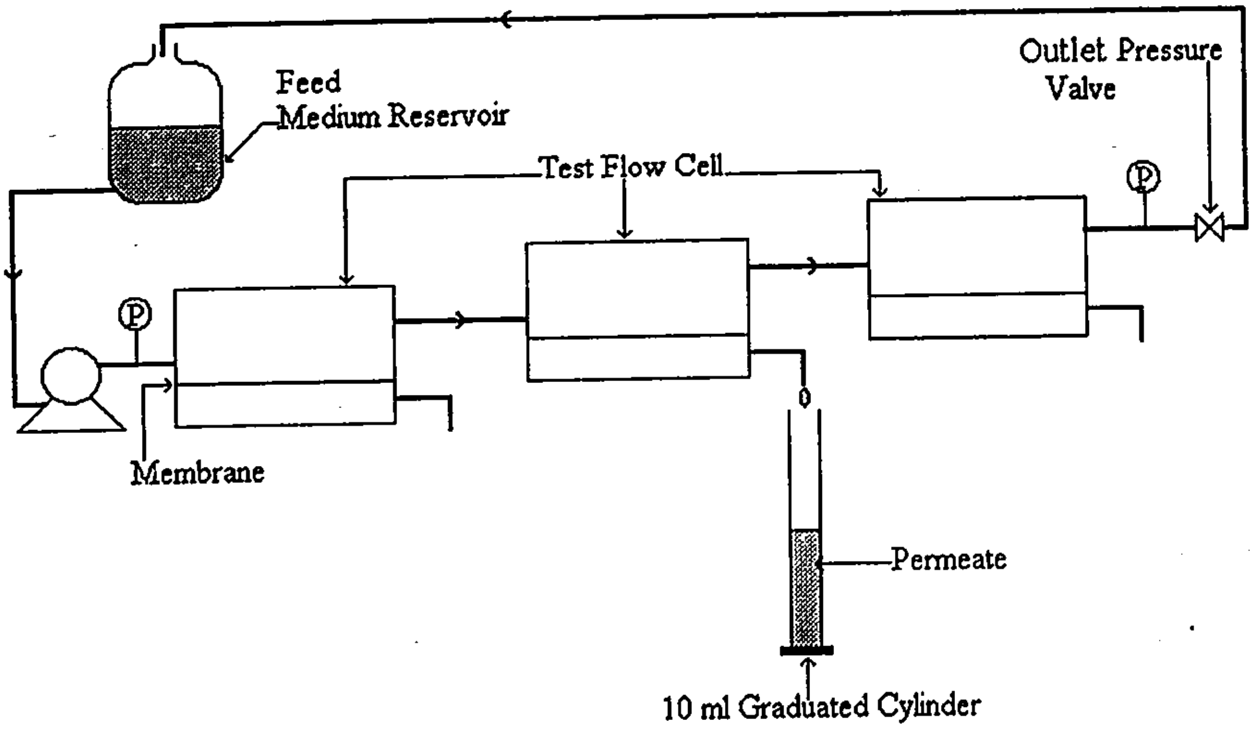

Figure 3.3. Schematic diagram of the apparatus used for the membrane characterization experiments.

manipulating the outlet pressure valve. The pump was set to a flow rate of 5.83×10^{-7} m^3/s (35 mL/min.), representative of flow rates used in the rectilinear flow cell. The first 10 mL of water permeate collected were discarded in order to measure steady state permeation rates. Water permeate was then collected in 10 mL graduated cylinders for one hour. Each set of experiments was repeated in triplicate, for a given overall pressure drop. Note that the rejection of the first 10 mL of permeate was only done when the outlet pressure was varied, and not between replicates. The experiments with deionized water were carried out at 103839, 105218, 106735, 110182, 116526, 124179, 130384 and 136659 Pa gauge (0.2, 0.4, 0.6, 1, 2, 3, 4 and 5 psig) for coupons labelled 4, 5 and 6 in Figure 3.2. This pressure range was thought to be representative of the pressures prevalent in the rectilinear flow cell. The barometric pressure was also measured with a mercury manometer in the Chemical Engineering Department's pilot plant for the subsequent calculation of the overall pressure drop across the three test cells. A sample calculation of membrane permeability is provided in Appendix B.

It was also of interest to determine whether or not exposure of the membrane to the previously increasing pressures affected the permeability. This was achieved by repeating the experiments with deionized water for decreasing pressures. For coupons 4, 5 and 6, the outlet pressure was set to 123834, 109424, 107217 and 104666 Pa gauge (3, 1, 0.6 and 0.2 psig) and the volume of permeate collected for a given overall pressure drop was recorded. These experiments were also performed in triplicate.

The next set of experiments consisted of determining the membrane permeability after the membrane coupons were exposed to a solution of BSA. For this purpose, a 7 kg/m^3 BSA solution was prepared. This concentration of protein represented an intermediate concentration to be used in the polarization experiments. The protein solution was recirculated for 36 hours to condition the membrane. Following the 36 hour conditioning period, permeability tests with deionized water were repeated at outlet pressures of 105631, 117905 and 137279 Pa gauge (0.4, 2 and 5 psig). Once again, the effect of subjecting the membrane coupons to decreasing pressures was studied at outlet pressures of 117146 and 105218 Pa gauge (2 and 0.4 psig). This completed the characterization of coupons 4, 5 and 6.

Coupons 1, 2 and 3 were subsequently placed in the three test cells. Permeability tests with deionized water were carried out at outlet pressures of 105218, 110527, 124662 and 138038 Pa gauge (0.4, 1, 3 and 5 psig), as described above for coupons 4, 5 and 6. The effect of decreasing pressure was investigated at 124593, 109837 and 105562 Pa gauge (3, 1 and 0.4 psig), in descending order.

In the next set of experiments, coupons 1, 2 and 3 were conditioned for 36 hours with a solution of sodium azide and 0.01 M phosphate buffer which formed the solvent phase for the BSA solutions. Permeability tests were performed at outlet pressures of 105356, 109837, 121697 and 135142 Pa gauge (0.4, 1, 3 and 5 psig). These coupons were then conditioned with a 7 kg/m^3 BSA solution for 36 hours. The sodium azide/phosphate buffer solution was then used to evaluate the permeability at 106666, 118249 and 138658 Pa gauge (0.4, 2 and 5 psig). The effect of decreasing pressure on the membrane coupons was then observed at 118663 and 106735 Pa gauge (2 and 0.4 psig).

The ability of the cellulose acetate membrane to retain BSA on the feed side of the test cells was determined by circulating 7 kg/m^3 BSA at the highest outlet pressure of 138658 Pa gauge (5 psig). The permeate was collected at the end of one hour for each of the six coupons and was then analyzed by HPLC techniques to quantify the protein, if any, which had permeated through the membrane. In addition to the permeate, samples of the protein feed solution prior to and following each retention test were also analyzed. The results of these tests are presented in Section 5.1.

3.3 Experimental Procedure for HPLC

Samples obtained from the flow cell were to be analyzed for albumin concentration using a Waters High Pressure Liquid Chromatography (HPLC) system in conjunction with a photodiode array detector (PDA) operating at 280 nm. Operating variables such as the use of a column versus a union, composition of mobile phase, use of a dye, size of the sample vials, volume of sample injected and column temperature were all components of the HPLC procedure which needed to be reviewed to accurately and precisely quantify albumin concentrations. Concerns associated with some of these operating variables will be briefly presented.

The use of a chromatographic column versus a union to quantify albumin concentrations was a concern. Since samples obtained from the flow cell could be considered pure albumin solutions, the separation ability of the column was not required. Furthermore, the combination of the HPLC column with a Coomassie Blue dye reagent proved incompatible due to interactions between the column and the dye. The use of a Coomassie Blue dye reagent could have enhanced the PDA response, enabling the quantification of dilute albumin samples. Alternatively, the use of the union would permit the composition of the mobile phase to be identical to the solvent employed in the flow cell. However, the main concern with the union was its ability to provide sufficient back pressure required to obtain reproducible chromatograms. The back pressure can be increased in two ways. Firstly, a long piece of HPLC tubing in the form of a restrictor could be inserted between the union and the outlet of the autosampler. Secondly, the use of a column, instead of a union, would also substantially increase the back pressure. Due to large errors in reproducibility between injections with the union, a column was used instead. The use of a column however precluded the opportunity to enhance the PDA response with a dye.

Experimental evidence indicated that operating variables such as sample vial size and injection volume significantly influenced the precision of the HPLC system. The use of 250 μL inserts resulted in a relative error of approximately 10 to 15% between multiple injections from a single vial whereas the 4 mL vials reduced the relative error to approximately 2%. However, the use of the 4 mL vials with their greater residual volumes necessitated the dilution of samples and required larger sample volumes to be withdrawn from the flow cell. While the 4 mL vials afforded a greater injection volume which further improved the precision of the HPLC system, the constraint of limiting the total sampling volume from the flow cell to about 2% could no longer be met.

A summary of the experimental procedure for determining albumin concentrations using a Waters HPLC system will now be presented. A Waters DE-613 column was used with a mobile phase composed of 70% acetonitrile, 30% deionized water and 0.1% trifluoroacetic acid, with the pump operated in the isocratic mode. A column temperature of 313.15 K (40 °C) was maintained. Albumin samples of 25 μL were diluted to 2 mL with the mobile phase, in 4 mL vials using an Eppendorf pipette. The run time for the samples in the HPLC system was 3 minutes. An injection delay of 10 minutes was specified between four injections to rinse the previous solution sample from the column. A calibration curve was generated using seven standards and a quadratic curve fit was found to be most accurate in the quantification of test BSA samples over the anticipated concentration range of the experiments. Standards were injected regularly to account for electronic drift in the HPLC instruments. The experimental protocol outlined above for quantifying BSA samples yielded a relative error up to 2% between multiple injections from the same vial.

3.4 The Procedure For Performing the Flow Experiments

The polarization of albumin was observed following 12, 24 and 36 hours of operation. A schematic diagram of the experimental apparatus used in the polarization study is shown in Figure 3.4. After the rectilinear flow cell was assembled, the lower chamber was filled with a solution of phosphate buffer containing 0.1 wt% sodium azide. The phosphate buffer was used to maintain the pH of the solution at 7.2 and the sodium azide was used as an anti-bacterial agent. The upper chamber was subsequently filled with a solution of albumin. The desired concentration of the protein was achieved by dissolving crystalline BSA in a solution of phosphate buffer/sodium azide which was identical to the solution in the lower chamber. The risk of developing air bubbles within the chambers was imminent during filling of the chambers. Therefore, the downstream section of the flow cell was raised during filling of the upper and lower chambers, in order to displace the air from the channel. Any air pockets persisting in the sampling ports were removed by continuous circulation of fluid in the upper chamber.

A typical experiment began by circulating the protein solution in the upper chamber for a period of 6-8 hours to achieve a uniform protein distribution along the reactor length. Circulation in the upper chamber was performed at a low flow rate to avoid the buildup of pressure which can lead to displacement of the sampling port capillaries. A flow rate in the range of 8.33×10^{-8}-$1.67\times^{-7}$ m^3/s (5-10 mL/min.) proved sufficient. Once the protein circulation was completed, the system was left at rest for approximately 3 hours to allow any remaining protein gradients to dissipate. After the pump was turned off, the inlet and outlet valves to the upper chamber were closed to seal the system.

The initial loading concentration of albumin in the upper chamber was determined by obtaining 3×25 μL samples from three sampling ports along the length of the flow cell. Hamilton syringes with a 25 μL capacity were inserted into the sample ports to withdraw the protein samples from the upper chamber. One sample was taken from the upstream portion of the cell, another from the middle and the last sample was withdrawn from the downstream region of the cell. Quantification of these protein samples was necessary to determine the magnitude of the initial loading concentration in addition to verifying that the concentration of albumin was uniform along the length of the channel. The protein samples obtained from the flow cell were diluted and analyzed for their concentrations using the HPLC procedure summarized above.

If the results of the HPLC analysis confirmed a uniform protein distribution along the length of the cell, the polarization experiment was started. Luminal fluid was circulated at the desired flow rate in the lower chamber for 12, 24 or 36 hours. At the end of the flow period, 25 µL protein samples were withdrawn from 8 to 10 sampling ports along the length of the flow cell. The diluted protein samples were stirred in 4 mL vials on a vortex mixer for 2 minutes. These samples were then quantified for their albumin concentrations using the HPLC system.

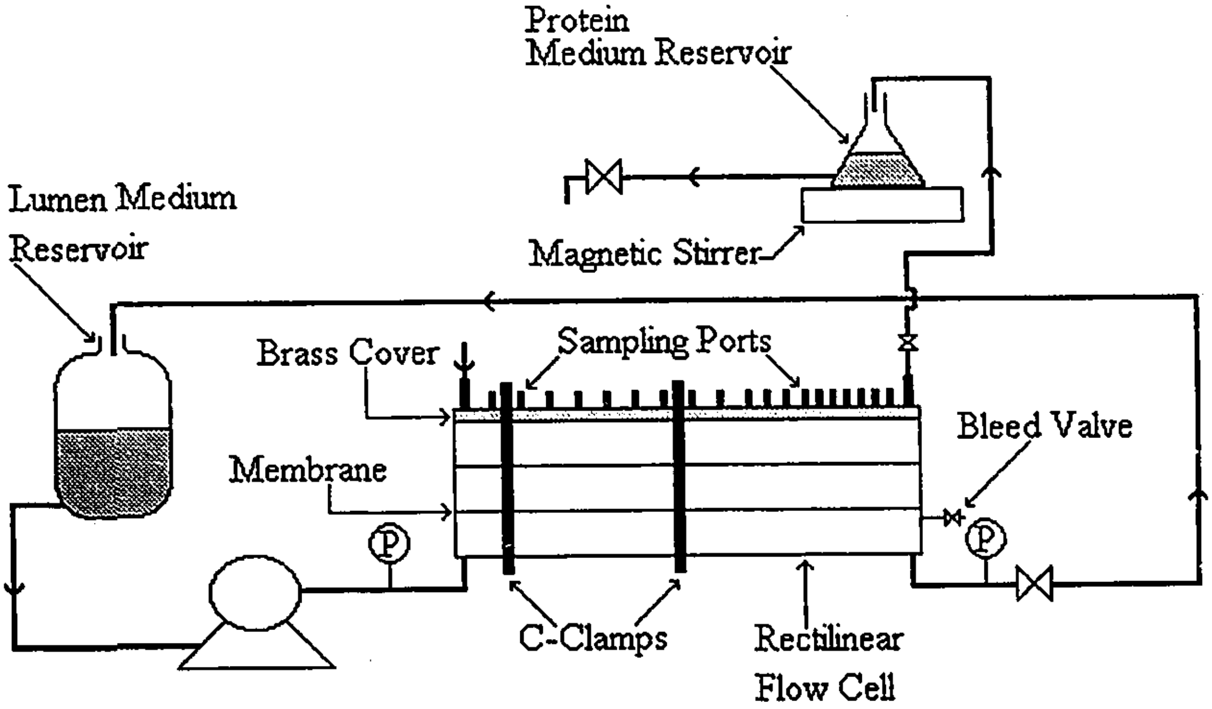

Figure 3.4. Schematic representation of the apparatus used to conduct polarization experiments.

4. PROPERTIES OF MATERIALS

The SEPA-SG13 cellulose acetate membrane was purchased from Osmonics, Inc. The membrane was obtained as a 0.65 m by 3 m flat sheet with a molecular weight cutoff between 1000-5000 Da. The membrane was stored in a solution of 0.5% v/v formaldehyde (HCHO). The formaldehyde was supplied by BDH and had a specified purity of 36.5-38% and boiling point of 96 °C.

The HPLC system, purchased from Millipore, was used to quantify concentrations of bovine serum albumin. The mobile phase used for the HPLC system consisted of acetonitrile (C_2H_3N), trifluoroacetic acid (CF_3COOH) and deionized water. The Omnisolv, HPLC grade acetonitrile supplied by BDH had a purity of 99.9% and a boiling point of 81 °C. Trifluoroacetic acid was purchased from BDH and had a specified purity of 99.7%. The 18 MΩ, deionized water was obtained from a Milli-Q system. The HPLC system also required the use of zero grade helium to sparge the mobile phase. The helium was supplied by Air Products Canada Ltd. A solution of 10 % v/v methanol was used by the HPLC system to rinse the autosampler syringe between injections. The HPLC grade methanol was obtained from Aldrich and had a purity of 99.9+% and a boiling point of 65 °C. The chromatographic column used in the HPLC system was a Shodex, DE-613 column purchased from Millipore. The HPLC column was packed with polymethacrylate gel.

Bovine serum albumin (BSA) was the solute used in the polarization study. Pentex grade, crystallized BSA was purchased from Miles Inc. and stored between the recommended temperature range of 2-8 °C. Some properties of the white BSA crystals are shown in Table 4.1. The BSA was dissolved in a solution of phosphate buffer and sodium azide (NaN_3). The phosphate buffer was supplied by Sigma Diagnostics at a concentration of 1.0 mol/L and a pH of 7.4 at 25 °C. The buffer was diluted to 0.01 mol/L with deionized water prior to the addition of BSA. The sodium azide, used as an anti-bacterial agent, was purchased from J.T. Baker Chemical Company in the form of a white powder with a specified purity of 95%. The required amounts of sodium azide and BSA were weighed with a Mettler analytical balance.

The density and viscosity of the phosphate buffer/sodium azide solution were experimentally determined. The density was measured to be 999.1 kg/m^3 using a densitometer. The viscosity of the phosphate buffer/sodium azide solution was measured to be 0.861 mPa• s using a Cannon-Fenske viscometer.

Table 4.1. Properties of bovine serum albumin (Taylor et al., 1994; Miles Inc. Manufacturer).

Molecular Weight	69 000 kg/kmol
Diffusivity in 0.1 M NaCl	1×10^{-10} m^2/s
Isoelectric Point	5.1
Solubility in water	585 kg/m^3
Temperature of Denaturation	50-60° C

5. RESULTS AND DISCUSSION

The problem of polarization in hollow fiber bioreactors is particularly pronounced with high molecular weight compounds such as albumin and has previously been observed by several researchers (Patkar et al., 1994; Waterland et al., 1975; Piret and Cooney, 1990b). The notably high Peclet numbers favour convective transport of high molecular weight substrates relative to diffusive transport resulting in polarization towards the downstream region of hollow fiber bioreactors. Further, gradients introduced by downstream polarization of proteins, cells and valuable byproducts should be minimized for the efficient operation of the reactors.

The objective of this research project was to investigate the phenomenon of concentration polarization of albumin within a rectilinear flow cell. A large portion of the research was devoted to the design and construction of the flow cell which could be used for future work. As discussed earlier, several modifications of the flow cell design were attempted in order to secure a leak free system. The fabrication of the flow cell was followed by the development of an appropriate experimental protocol for the acquisition and analysis of albumin samples. Various aspects of the HPLC system had to be resolved, including the use of a column or a union, composition of the mobile phase, sample vial size and sample size. Transient polarization of BSA was subsequently investigated following 12, 24 and 36 hours of operation. The experimental results were compared to those predicted by a mathematical model developed by Taylor and coworkers (1994).

5.1 Membrane Characterization

The membrane was characterized to provide an accurate measure of its permeability as well as for verifying that the membrane was impermeable to the albumin. An ultrafiltration, cellulose acetate membrane was used to retain the albumin in the upper chamber of the flow cell while allowing the exchange of a solution of phosphate buffer and sodium azide. The membrane was obtained as a large flat sheet and characterization of the membrane was performed in the region from which a strip was cut for use in the flow cell. Six coupons were tested from a cross-section of the membrane; the locations of these coupons are illustrated in Figure 3.2 and are denoted as coupons 1, 2, 3, 4, 5 and 6. The membrane coupons were tested for permeability, hysteresis in the membrane permeability due to changing pressure drops across the coupons, albumin binding and aging effects.

From a plot of the permeation rate versus the pressure drop across the membrane coupon, the permeability of the membrane divided by the viscosity of the feed solution was evaluated; that is, the slope from such a plot is equal to L_p/μ. In this research, the quantity L_p/μ is one of the parameters used in the FORTRAN program and is hence more convenient than the permeability, L_p. Henceforth, the quantity L_p/μ will be referred to as the membrane permeability. A measure of L_p/μ for coupons 1, 2, 3, 4, 5 and 6 was determined with 18 MΩ, deionized water as the feed to the test flow cells. The data obtained with deionized water are graphically shown in Figure 5.1. Each datum point represents the average permeation rate of three experiments. The experimental data used to determine the permeability for the membrane coupons are tabulated in Appendix A. Table 5.1 illustrates the values of the permeability for coupons 1 through 6. The correlation coefficients for the data shown in Figure 5.1 are given in Table 5.1. The calculations to evaluate L_p/μ for the case of the deionized water feed are found in Appendix B.

The value of L_p/μ for the six membrane coupons varied between 2.80×10^{-11} and 8.19×10^{-11} m^2s/kg, as illustrated in Table 5.1. In addition to providing an estimate of the membrane permeability, the deionized water experiments served to demonstrate local variability in the permeability of the membrane. However, the location of the membrane coupons was not used to predict the variability in the membrane permeability; that is, no correlation was sought between the membrane permeability and coupon location.

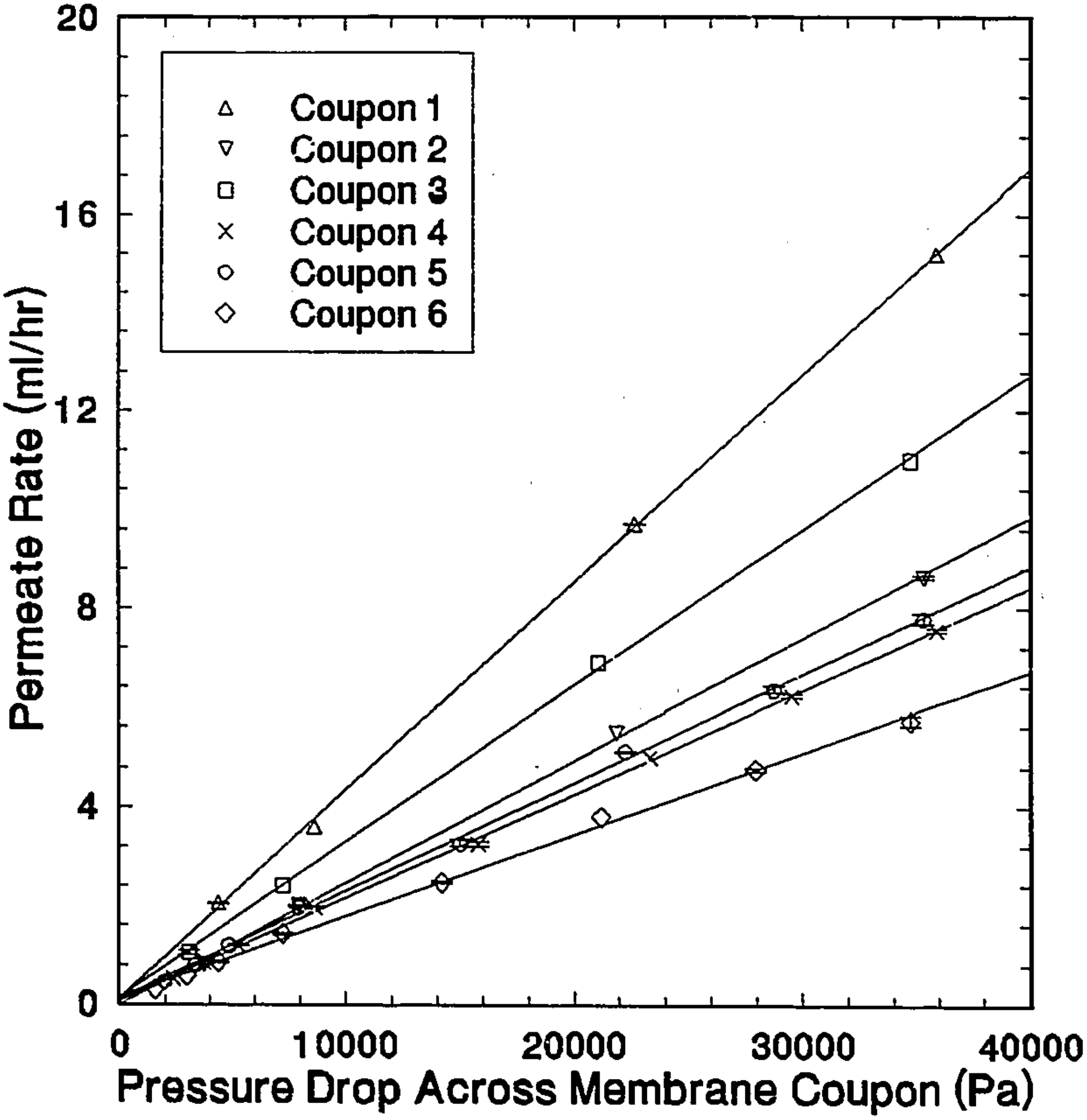

Figure 5.1. Plot of permeation rate data obtained with deionized water for coupons 1-6.

In addition to these permeability experiments, hysteresis in the membrane permeability was investigated. The permeability of deionized water was determined by increasing the pressure across the membrane between 1379 Pa gauge (0.2 psig) and 34474 Pa gauge (5 psig). Next, the permeability was evaluated by decreasing the pressure across the membrane, over the pressure range cited above. Hysteresis effects could be verified by comparing the permeabilities obtained by increasing and decreasing the pressure across the membrane. The hysteresis experiments were conducted with the six coupons and the results are shown in Table 5.1. A typical hysteresis plot is illustrated for coupon 4 in Figure 5.2. Hysteresis plots for the remaining coupons are included in Appendix B. Figure 5.2 and Table 5.1 demonstrate that there were no significant hysteresis effects due to pressure since the slopes for increasing and decreasing pressures were nearly identical. Therefore, the membrane permeability would not be expected to vary with fluctuations in the operating pressure range typical of the rectilinear flow cell.

Table 5.1. Results of L_p/μ obtained with deionized water for the six membrane coupons.

Coupon	L_p/μ as pressure is increased, ($\times 10^{11}$) m^2s/kg	Correlation coefficient for increasing pressure	L_p/μ as pressure is decreased, ($\times 10^{11}$) m^2s/kg	Correlation coefficient for decreasing pressure
1	8.19	0.9997	8.35	0.9999
2	4.81	0.9992	4.79	1.0000
3	5.44	0.9996	5.43	1.0000
4	3.89	0.9994	3.88	0.9998
5	3.81	0.9988	3.77	0.9996
6	2.80	0.9977	2.85	0.9999

It was also of interest to determine the susceptibility of the membrane to albumin binding and subsequent fouling. The protein fouling experiments exposed the membrane coupons to a solution of albumin for 24 hours, to condition the membrane. The permeability of deionized water was then determined after conditioning coupons 4, 5 and

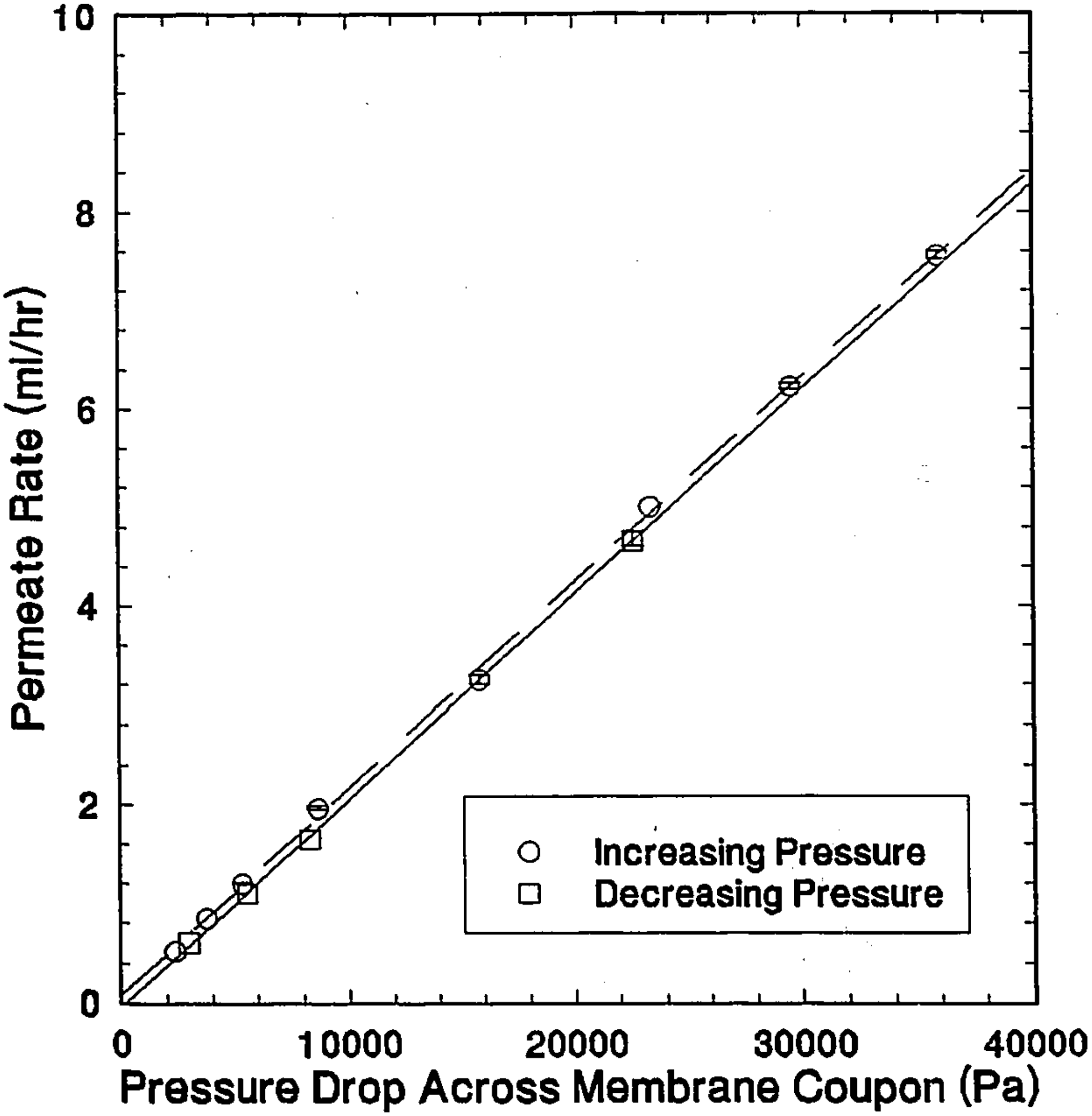

Figure 5.2. Plot of permeation rate data obtained with deionized water to investigate hysteresis in the membrane permeability due to increasing and decreasing pressures for coupon 4.

6 with a solution of 7 kg/m^3 BSA. Once again, plots of permeation rate versus the pressure drop across the membrane coupons were utilized to calculate the permeability of the membrane to deionized water. Figure B.3, Appendix B illustrates the results of the fouling experiments. The permeability for coupons 4, 5 and 6 decreased by approximately 30% after the coupons were conditioned with a solution of BSA, as seen by comparing the results tabulated in Tables 5.1 and 5.2. This suggested that albumin adsorbed to the surface of the cellulose acetate membrane thereby decreasing its permeability. Hysteresis in the membrane permeability, following exposure of the membrane coupons to a solution of albumin protein was also studied. As shown in Table 5.2, the effect of decreasing the pressure was negligible on the permeability of the membrane. Therefore, the permeability of the membrane was not influenced by cyclic pressure changes. The correlation coefficients for the case of decreasing pressures in Table 5.2 are unity since two data points were used to evaluate the slope of the plots given in Figure B.3, Appendix B.

Table 5.2. Results of L_p/μ obtained with deionized water for increasing and decreasing pressures for coupons 4, 5 and 6 following exposure to a solution of BSA.

Coupon	L_p/μ as pressure is increased, ($\times 10^{11}$), m^{2}s/kg	Correlation coefficient for increasing pressure	L_p/μ as pressure is decreased, ($\times 10^{11}$), m^{2}s/kg
4	2.76	0.9997	2.79
5	2.75	0.9999	2.88
6	1.96	0.9998	2.01

The permeability of the membrane to the solvent solution was also tested. In particular, the membrane permeability for coupons 1, 2 and 3 was determined with a solution of phosphate buffer and sodium azide prior to and following exposure of these coupons to a solution of 7 kg/m^3 BSA. The plots of permeation rate versus pressure drop across the membrane coupons are shown in Figure B.3, Appendix B and the permeabilities are given in Table 5.3.

The permeability of these coupons to the phosphate buffer/sodium azide solution, prior to conditioning with the protein solution, is approximately 6 to 12% lower than the corresponding permeability for deionized water, as is evident by comparing values of L_p/μ in Tables 5.1 and 5.3. The permeability of the membrane to the solution of phosphate buffer and sodium azide is about 17 to 20% lower, meanwhile, after conditioning with protein as compared to that before exposure to the albumin solution.

Table 5.3. The permeability results for coupons 1, 2 and 3 using phosphate buffer/sodium azide solution, prior to and following exposure to a solution of BSA.

Coupon	L_p/μ before conditioning with BSA, ($\times 10^{11}$), m^2s/kg	Correlation coefficient before BSA conditioning	L_p/μ after conditioning with BSA, ($\times 10^{11}$), m^2s/kg	Correlation coefficient after BSA conditioning
1	7.73	0.9997	6.45	0.9996
2	4.36	0.9993	3.72	0.9997
3	4.87	0.9989	4.14	0.9996

The results of the hysteresis experiments following protein conditioning of coupons 1, 2 and 3 are shown in Table 5.4. The hysteresis plots for coupons 1, 2 and 3 are included in Appendix B. The effect of decreasing the pressure drop across the membrane coupons on the membrane permeability was found to be negligible. Table 5.4 contains the permeabilities of coupons 1, 2 and 3 as a function of increasing and decreasing pressures. Again, the correlation coefficients for the case of decreasing pressures given in Table 5.4 were unity since the plot was constructed from two data points.

Table 5.4. Permeability results obtained with increasing and decreasing pressures for coupons 1, 2 and 3 following exposure to a solution of BSA.

Coupon	L_p/μ as pressure is increased, ($\times 10^{11}$), m^2s/kg	L_p/μ as pressure is decreased, ($\times 10^{11}$), m^2s/kg
1	6.45	6.56
2	3.72	3.71
3	4.14	4.17

The permeability of the cellulose acetate membrane was evaluated as the average of the permeabilities determined following protein conditioning: 3.63×10^{-11} m^{2}s/kg. This value of the permeability was used in the theoretical model to predict the concentration profiles of BSA for comparison with the experimental profiles. However, the permeability of the membrane may vary with time. Aging tests were therefore performed five months after the initial permeability tests during which time, the membrane coupons were stored in 0.5% v/v formaldehyde solution. The aging tests were performed with coupons 1, 2 and 3, in which the permeability of the membrane was again determined with the solution of phosphate buffer and sodium azide. The results of the aging tests are given in Table 5.5 and a graphical representation is shown in Figure B.4, Appendix B. The aging tests show that the permeability of the membrane after five months of storage varied from about 4 to 10%. Therefore, the effects of aging were considered minimal in comparison to the magnitude of the local variability in the membrane permeability.

Table 5.5. Results of the aging tests to determine the permeability of coupons 1, 2 and 3.

Coupon	L_p/μ, ($\times 10^{11}$), m^{2}s/kg	L_p/μ after 5 months of storage, ($\times 10^{11}$), m^{2}s/kg	Correlation coefficient after 5 months of storage
1	7.73	7.19	0.9964
2	4.36	4.81	0.9983
3	4.87	4.67	0.9988

Characterization of the membrane also served to verify that the membrane was impermeable to BSA, enabling the protein to be retained within the upper chamber of the flow cell. Samples of the permeate obtained from the test flow cells for the six membrane coupons were analyzed for BSA concentration using HPLC techniques. A chromatogram representative of a protein free sample is shown in Figure 5.3a. Figure 5.3b displays a chromatogram of a permeate sample obtained from coupon 4 and Figure 5.3c illustrates a chromatogram of a sample containing 1 kg/m^3 BSA. A comparison of the chromatograms of Figures 5.3a, 5.3b and 5.3c suggests that protein is absent from the

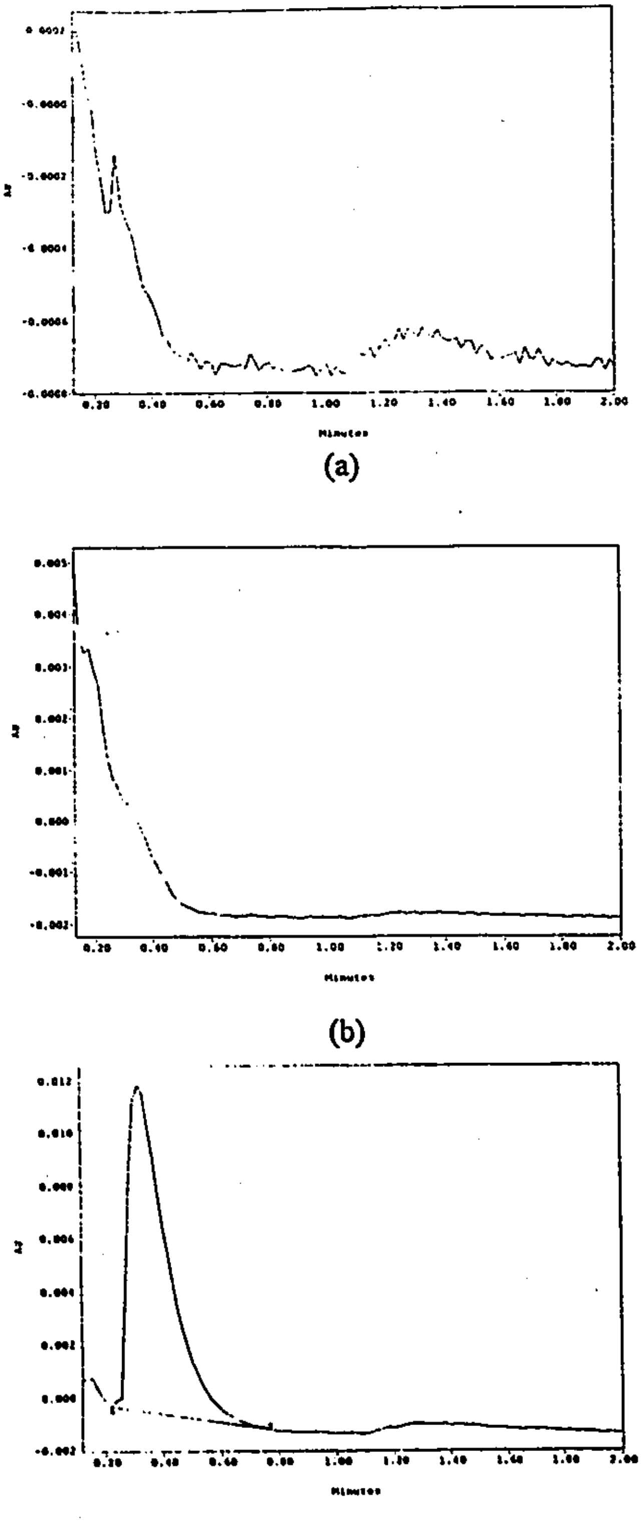

(a)

(b)

(c)

Figure 5.3. (a) Chromatogram of a protein free solution of phosphate buffer and sodium azide. (b) Chromatogram of the permeate sample obtained from coupon 4. (c) Chromatogram of a sample containing 1 kg/m^3 BSA.

permeate, indicating that the membrane successfully retains the protein. The scale for the protein peak in Figure 5.3c is an order of magnitude greater than that of the permeate sample shown in Figure 5.3b, illustrating that the permeate is virtually protein free. (Note that the permeate analyses were performed with a union.) Similar chromatograms were obtained for the permeate samples of the remaining five coupons. The results of these protein rejection tests are shown in Table 5.6. A rejection ratio of unity indicates that the membrane is capable of completely retaining the protein. The rejection ratios shown in Table 5.5 are close to unity so that, for the purposes of this study, the membrane may be considered impermeable to BSA.

Table 5.6. Rejection ratios for membrane coupons.

Coupon	Rejection ratio
1	0.9819
2	0.9711
3	0.9851
4	0.9903
5	0.9932
6	0.9965

In summary, local variations in the permeability of the membrane, from 2.8×10^{-11} to 8.19×10^{-11} m^2s/kg, were observed. In addition, the permeability of the membrane did not exhibit hysteresis effects due to pressure fluctuations. Furthermore, protein binding to the membrane surface resulted in a 17-20% decrease in membrane permeability, suggesting that the membrane strip used in the rectilinear flow cell be conditioned with BSA prior to performing the polarization experiments. Aging of the membrane had little effect on the permeability. Finally, the cellulose acetate membrane was found to be impermeable to BSA.

5.2 Polarization Study

The effect of osmotically active BSA on the hydrodynamics of a rectilinear flow cell was studied. This objective was fulfilled by investigating the polarization of BSA after 12, 24 and 36 hours of operation. The results of the polarization experiments are presented as concentration profiles of albumin in the extraluminal space, along the length of the rectilinear flow cell, as well as the concentration profile predicted from theoretical analysis. The transient polarization experiments were repeated three times, unless otherwise specified. The error bars shown for each data point represent the total variation in the average BSA concentration from three replicates of an experiment.

The concentration profiles obtained following 12, 24 and 36 hours of operation are shown in Figures 5.4, 5.5 and 5.6, respectively. The profiles based on the experimental results reveal low upstream concentrations and higher downstream concentrations, indicative of polarization of the protein towards the downstream region of the flow cell. The degree of polarization increases with time as seen by comparing the concentrations at a given distance along the reactor length. For example, at a distance of 0.5756 m (57.56 cm), the albumin concentrations after 12, 24 and 36 hours of operation were determined to be 9.19×10^{-1} kg/m^3, 1.23 kg/m^3 and 1.67 kg/m^3 while the initial loading concentrations were 6.50×10^{-1} kg/m^3, 6.91×10^{-1} kg/m^3 and 7.45×10^{-1} kg/m^3, respectively. Hence, at the downstream end of the cell, albumin was 1.41, 1.78 and 2.24 times more concentrated than the initial loading concentration after 12, 24 and 36 hours of operation, respectively.

The concentration distributions predicted from theoretical analysis are shown by solid lines in Figures 5.4, 5.5 and 5.6. The experimental data qualitatively agree with the theoretical prediction of polarization. However, the mathematical model seems to over predict the experimental concentration profiles of albumin for all three transient cases studied. In particular, the greatest deviation between the model and experiments

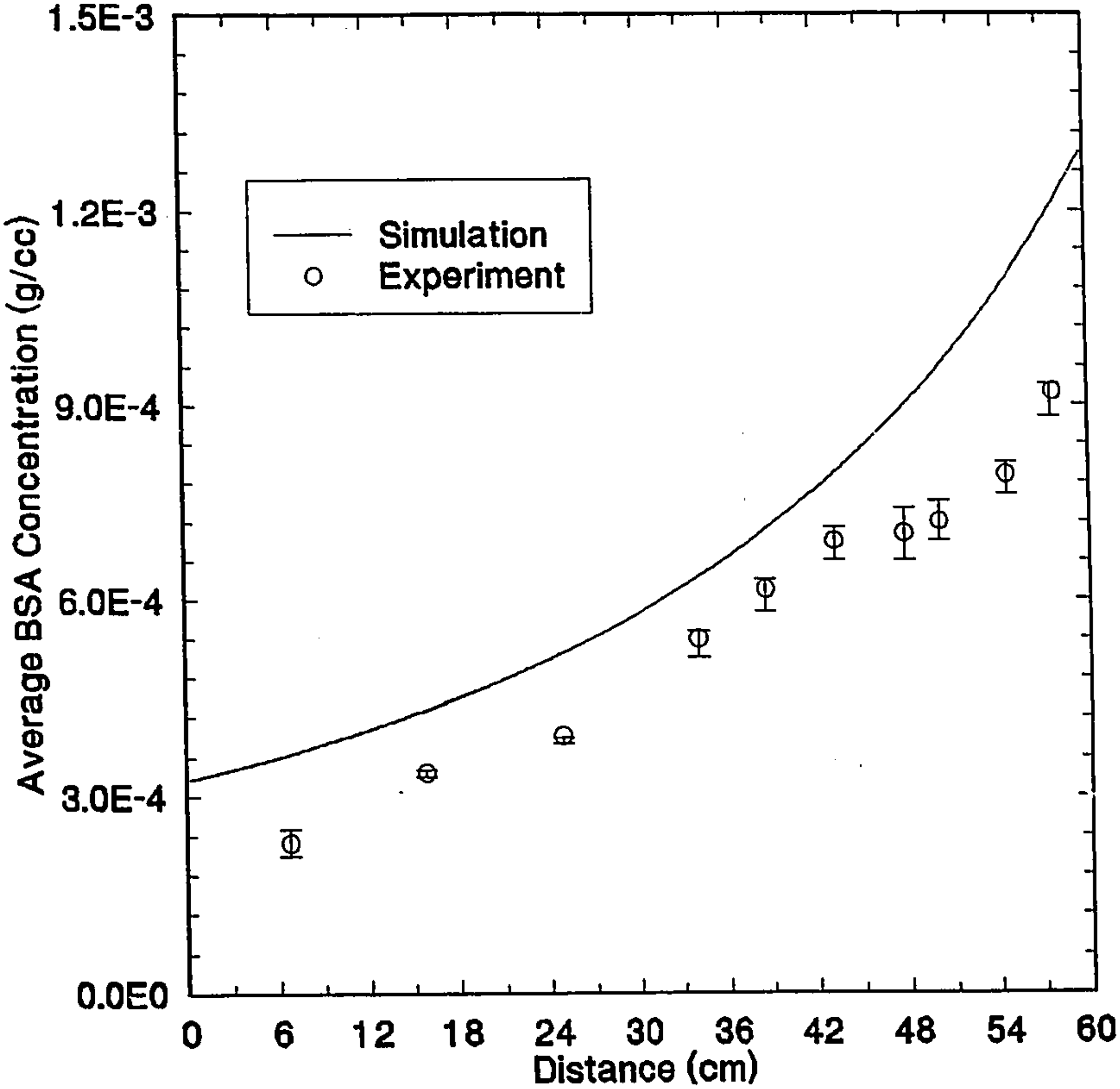

Figure 5.4. Transient concentration profile of BSA following 12 hours of operation with $C_{BO} = 6.5\times10^{-1}$ kg/m^3 and $\overline{u}_L = 0.12$ m/s.

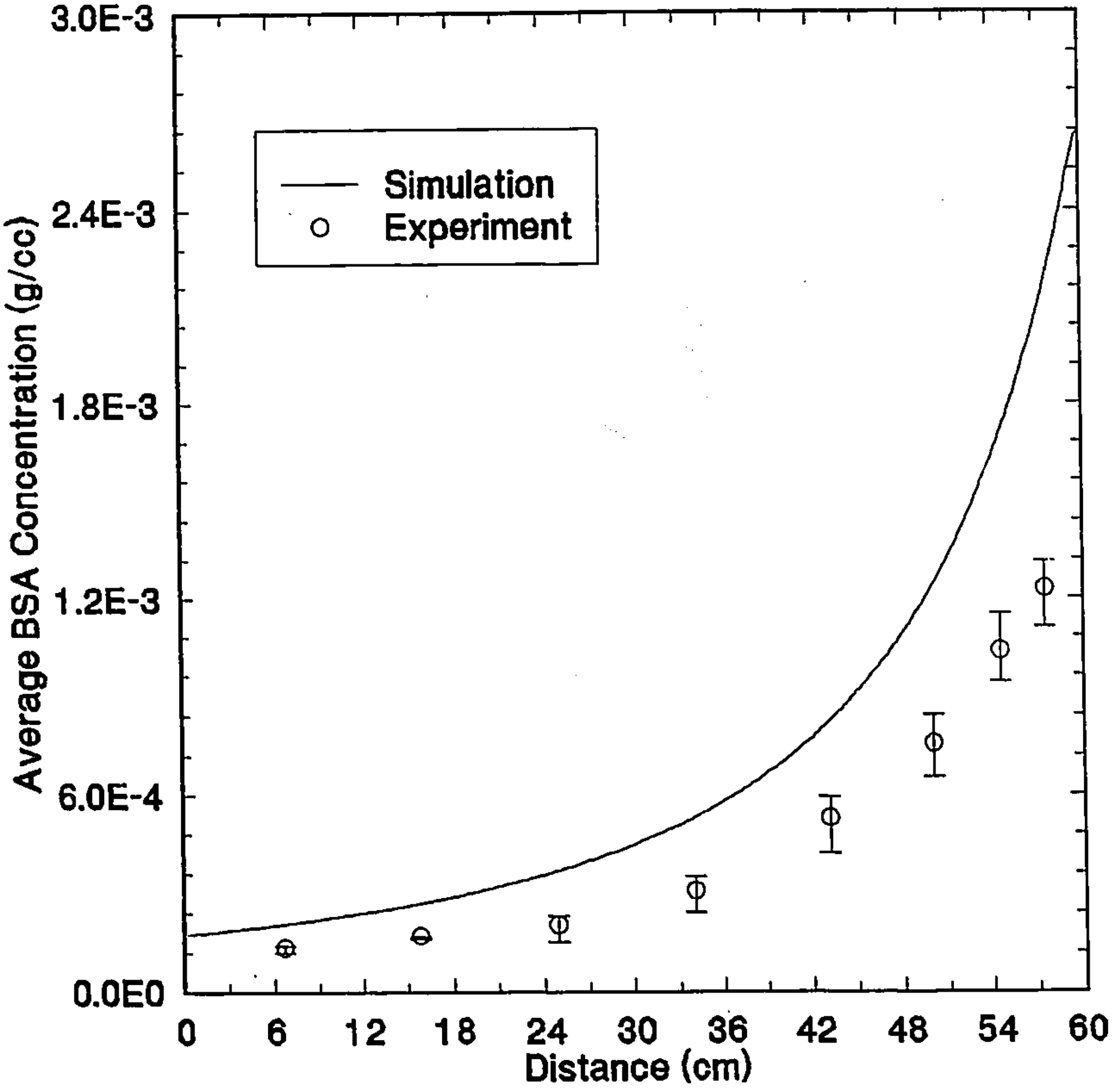

Figure 5.5. Transient concentration profile of BSA following 24 hours of operation with $C_{so} = 6.91\times10^{-1}$ kg/m^3 and $\overline{u}_L = 0.12$ m/s.

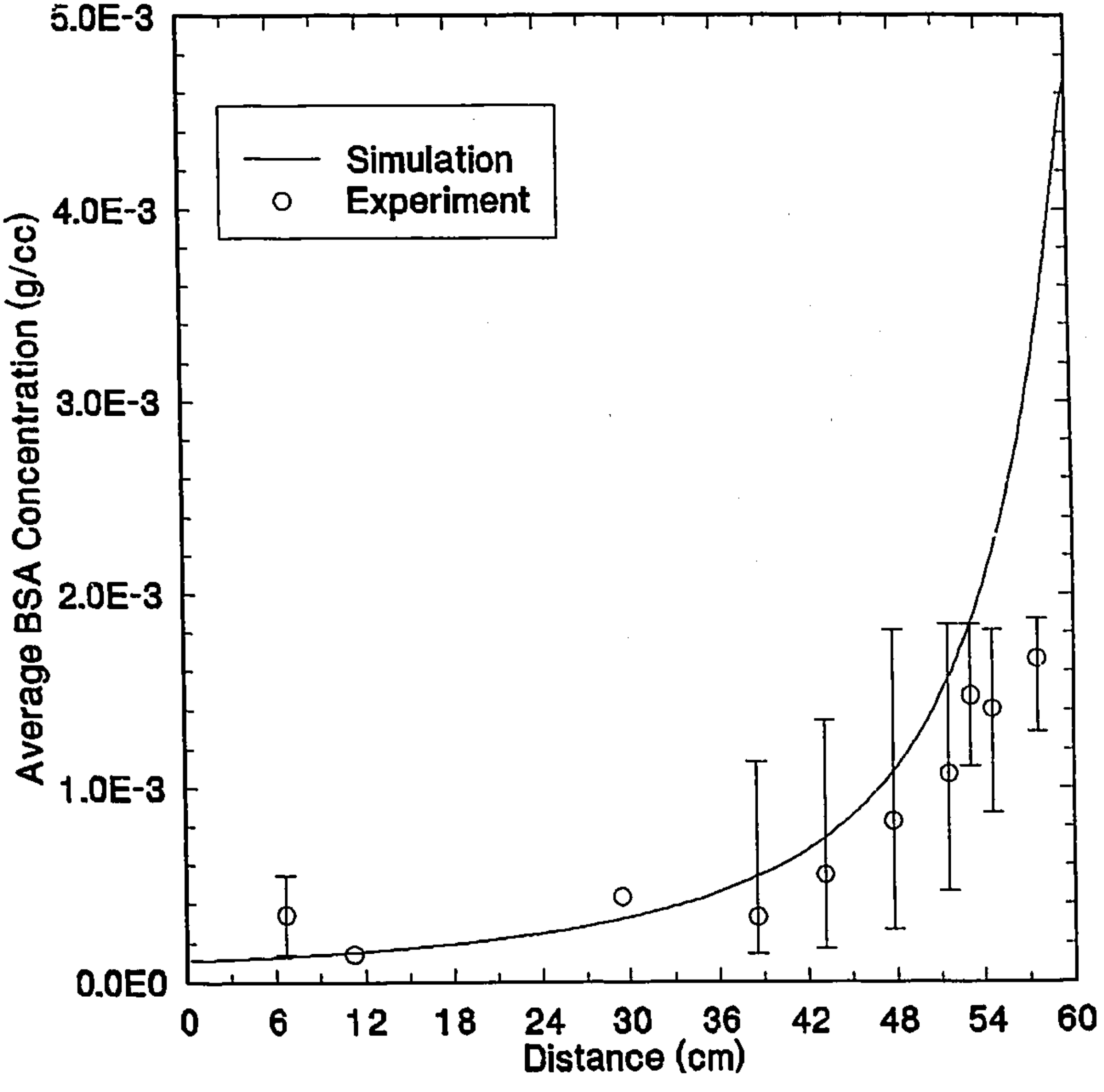

Figure 5.6. Transient concentration profile of BSA following 36 hours of operation with $C_{to} = 7.45\times10^{-1}$ kg/m^3 and $\overline{u}_L = 0.12$ m/s.

consistently occurred in the downstream region of the flow cell. Possible explanations for the disagreement between BSA concentration profiles predicted by the model and those BSA concentration profiles obtained experimentally will now be discussed. It was postulated that possible dilution effects during sampling as well as some assumptions in the theoretical model could account for the observed disagreement between predicted and experimental results. Therefore, additional experiments were performed in an attempt to resolve this discrepancy.

Dilution of the BSA samples obtained from the flow cell could have contributed to the discrepancy between the theoretical model and the experimental results. Since the model conserves mass, a concentration profile which consistently lies below the predicted one suggests the possible loss of protein. This loss could occur as a consequence of leaks or as a result of dilution during sampling. Since there were no visible leaks in the cell, the experimental procedure used to obtain the BSA samples from the flow cell was scrutinized further.

The first aspect of the experimental protocol which may have explained diluted samples was the introduction of protein free fluid from the lower chamber. Since the BSA samples from the upper chamber were withdrawn by means of gas tight syringes, it was possible that suction during withdrawal of the BSA samples would force fluid from the lower chamber into the upper chamber, thereby diluting the sample. Initially, during the transients polarization experiments, the inlet valve to the upper chamber was opened during sampling, while the outlet valve of the upper chamber was closed. This configuration enabled the volume of BSA solution withdrawn by the syringe to be preferentially replaced by upstream protein solution instead of the protein free solution from the lower chamber. It was believed that the hydraulic resistance of the membrane would be greater than the resistance experienced by the protein solution flowing through the upper chamber. Since dilution in the upstream portion of the flow cell was not as severe as in the downstream portion, it was thought that the problem of sample dilution at the downstream end of the reactor could be improved by opening the outlet valve of the upper chamber. A polarization experiment was then undertaken for 12 hours of operation and the concentration profile obtained with both the inlet and outlet valves opened, as shown in Figure A.1, Appendix A. The theoretical concentration profile still over predicted the concentration profile determined experimentally. Therefore, there was no advantage to be gained by opening the outlet valve.

Another possible source of apparent dilution was the potential for fluid mixing within the upper chamber during sampling. The opportunity for the fluid surrounding one sampling port to mix with fluid from an adjacent sampling port was believed to be particularly severe with large sampling volumes and between ports which were closely spaced. The sampling ports in the downstream region of the flow cell were closer in proximity than the upstream sampling ports and this geometrical arrangement was thought to possibly contribute to the dilution of samples in the downstream section. It was not feasible to reduce the sampling volume since the reliability of the HPLC procedure outlined in Section 3.3 for quantifying BSA samples depended upon obtaining 25 μL samples. Therefore, an experiment was performed for 12 hours of operation in which BSA samples from four well spaced sampling ports were taken. The concentration profile obtained with the fewer ports is illustrated in Figure 5.7. Again, the problem of apparent sample dilution persisted when fewer ports were sampled.

The possible variations to the experimental procedure used to obtain BSA samples from the flow cell proved unsuccessful in reducing the discrepancy between theoretical and experimental BSA concentration profiles. At this point, certain assumptions in the theoretical model were considered as sources of the deviation observed between the experimental and theoretical results. The theoretical model used here is a one-dimensional version of that of Taylor and coworkers (1994) which neglects transverse velocity, pressure and concentration gradients along the reactor length. The motivation for using the one-dimensional model originated from the success of Patkar et al. (1994) to model

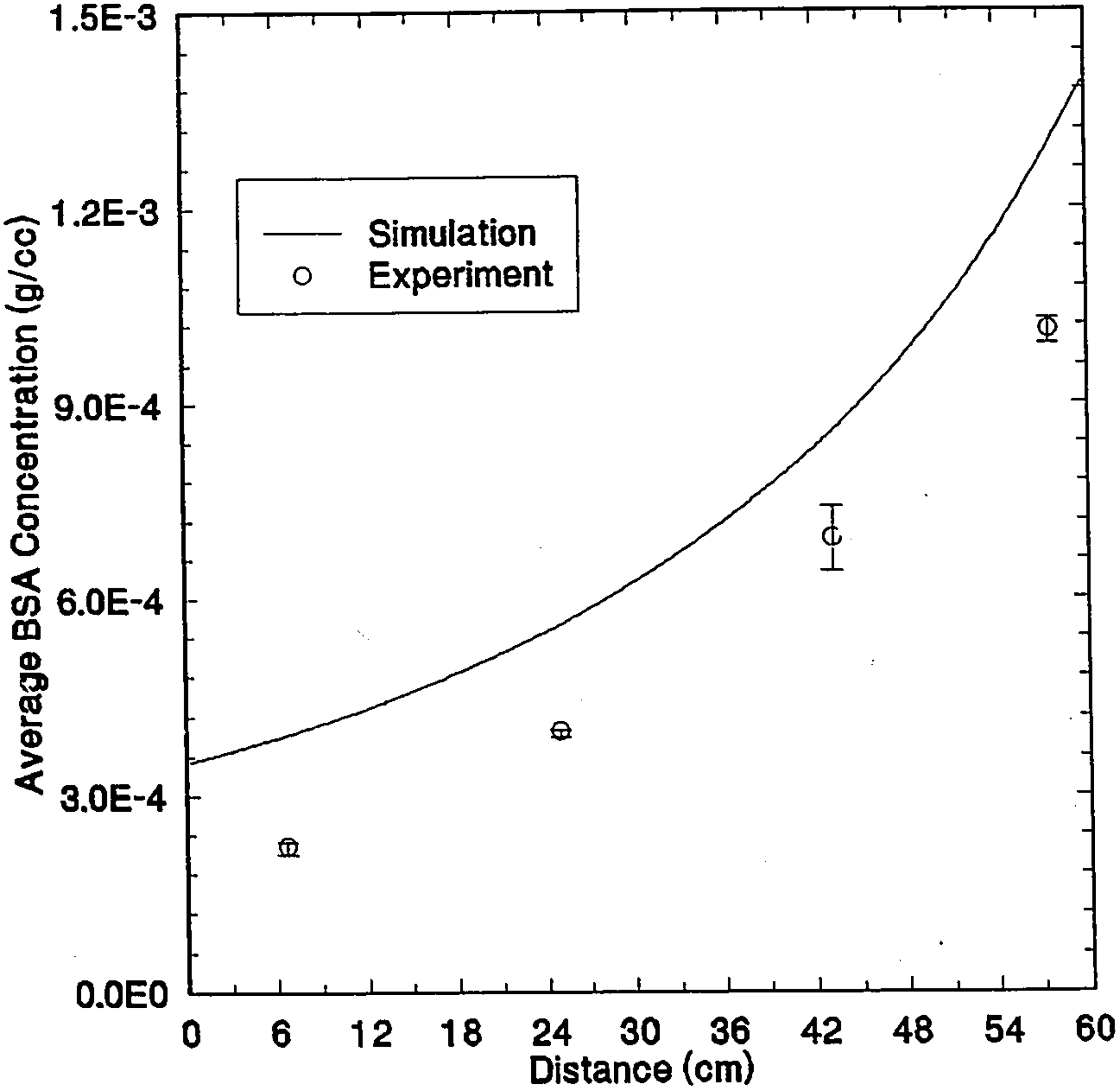

Figure 5.7. Transient concentration profile of BSA following 12 hours of operation obtained with four sampling ports, $C_{bo} = 7.01\times10^{-1}$ kg/m^3 and $\overline{u}_L = 0.12$ m/s.

protein distributions within hollow fiber bioreactors using the one-dimensional approximation of the three-dimensional system. The aspect ratio for the geometry of the hollow fiber used by Patkar et al. (1994) was 1.07×10^{-3}. This value of the aspect ratio is typical of a single fiber and surrounding extraluminal space characteristic of hollow fiber bioreactors. The aspect ratio of the flow cell used in this research project was 4.17×10^{-3}, which is of the same order of magnitude as that of the hollow fiber bioreactor functional unit.

A possible source of transverse gradients not accounted for in the theoretical model is the phenomenon of sedimentation. The albumin may sediment during the 12, 24 and 36 hours of operation. This would yield a concentrated layer of protein at the surface of the membrane and a correspondingly dilute solution of BSA in the sampling region of the cell. To test this hypothesis, sedimentation experiments were performed that consisted of allowing the BSA in the upper chamber to settle in the absence of flow in the lower chamber. The BSA samples were analyzed from three sampling ports, following 12 hours of settling time. The results of the sedimentation experiment are given in Table 5.7. The maximum relative difference between the initial and final concentrations was found to be about 3%. Since a typical relative difference between injections from a single vial was observed to be approximately 2%, the results suggest that sedimentation does not play a significant role in concentrating BSA at the membrane surface. Moreover, the final concentration after settling for 12 hours is actually greater than the initial concentration for two of the samples shown in Table 5.7. This further emphasizes the negligible contribution of sedimentation in generating transverse gradients.

Table 5.7. Results of sedimentation experiments following 12 hours of settling time.

Distance along reactor length, m	Initial concentration, (× 10), kg/m^3	Final concentration, (× 10), kg/m^3	Relative difference, %
0.1124	5.83 (±0.163)	5.90 (±0.007)	1.20
0.3404	5.90 (±0.156)	6.07 (±0.608)	2.88
0.5756	5.78 (±0.071)	5.66 (±0.042)	2.12

In addition, the assumption of a one-dimensional model may not be representative of the physical situation, particularly at the cell extremities, where end effects are prevalent. Furthermore, a significant error may be introduced into the theoretical model by neglecting transverse velocity gradients especially at higher velocities. Therefore, the importance of transverse velocities was studied by conducting an experiment at a low velocity, where the assumption of a one-dimensional model was thought to be most accurate. The velocity in the lower chamber was reduced from 0.12 m/s (12 cm/s) to 0.02 m/s (2 cm/s). Since the velocity was decreased, the polarization process was slower, hence the effect of decreasing the lower chamber velocity was studied following 48 hours of operation. The concentration profile obtained after 48 hours and with a velocity of 0.02 m/s (2 cm/s) is given in Figure 5.8. The experimental data points exhibit a random scatter about the theoretical BSA concentration profile instead of the consistently lower data of Figures 5.4 through 5.7. This suggests that the assumption of a one-dimensional theoretical model is more accurate at low velocities, where transverse velocity gradients are smaller. However, the theoretical model continues to over predict the BSA concentration profile at the downstream end of the flow cell, where protein packing adjacent to the membrane surface is likely the greatest.

One way to confirm the presence of transverse concentration gradients would be to withdraw BSA samples from different transverse locations in the upper chamber. To this end, the flow cell could be modified such that sampling is made possible from a concentrated layer near the membrane surface as well as from a correspondingly dilute layer near the top of the upper chamber, should such distinct layers exist. If protein packing occurs adjacent to the membrane surface, then samples withdrawn from the center of the chamber, as in the current work, would exclude some protein. Hence, these diluted samples would not be representative of the average BSA concentration, thereby explaining the consistently lower experimental profiles.

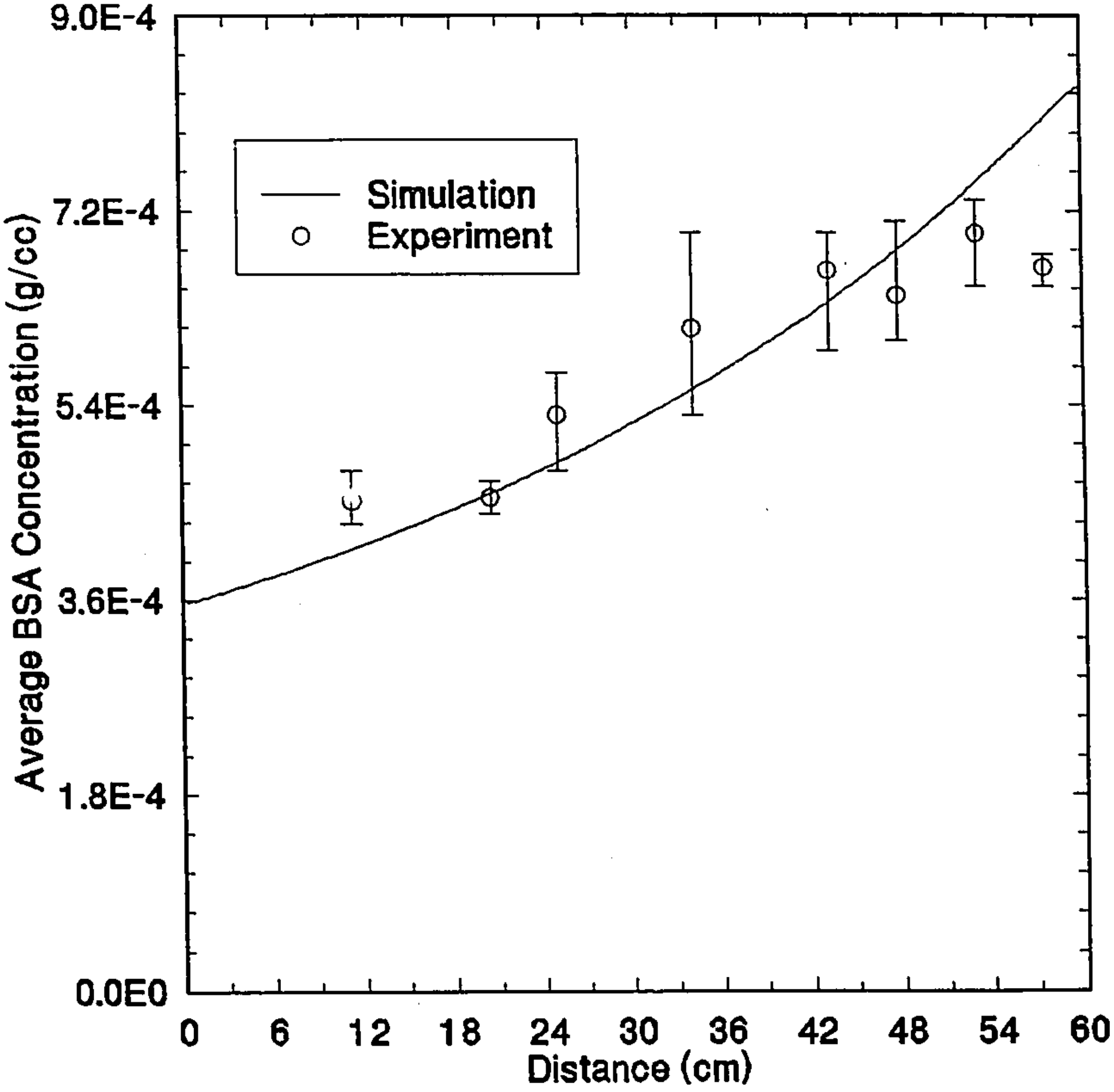

Figure 5.8. Transient concentration profile of BSA following 12 hours of operation with $C_{Lo} = 5.47\times10^{-1}$ kg/m^3 and $\overline{u}_L = 0.02$ m/s.

Another source for the discrepancy between the results predicted from theoretical analysis and those determined experimentally may be due to variations in the permeability of the cellulose acetate membrane from the experimentally determined average. The effect of the membrane permeability on the concentration profiles generated by the mathematical model is illustrated in Figure 5.9, which compares the theoretical concentration profiles of albumin using three different values for the permeability. The three permeabilities were selected from the results of the membrane characterization experiments and represent the high and low extremes in the experimentally determined permeabilities as well as the arithmetic average. Based on Figure 5.9, the degree of albumin polarization increases significantly as the permeability of the membrane increases so that the assumed value of the permeability strongly influences the concentration profiles predicted by the model. In fact, the simulation results using the lower permeability appear to agree more closely with the 36 hour experimental data, compared with the other two curves. However, the theoretical profiles generated using the low permeability for the 12 and 24 hour cases deviate for the upstream data yet reduce the discrepancy observed for the downstream data points. The situation may be further complicated by local variations in the permeability within the strip of membrane used in the flow cell, which could also account for the disagreement between model and experiment.

Given the preceding discussion, there are three recommendations which may be attempted in future work to reconcile the observed discrepancy between theoretical and experimental BSA concentration profiles: the development of a two-dimensional model for the rectangular duct geometry; the direct measurement of the permeability of the membrane strip used in the flow cell; and the operation of the flow cell in the vertical orientation. The theoretical model should be modified to include transverse gradients in velocity, concentration and pressure. A comparison of theoretical predictions generated from a two-dimensional model with experimental concentration profiles may reduce the discrepancy between the two. This recommendation is based on the experimental

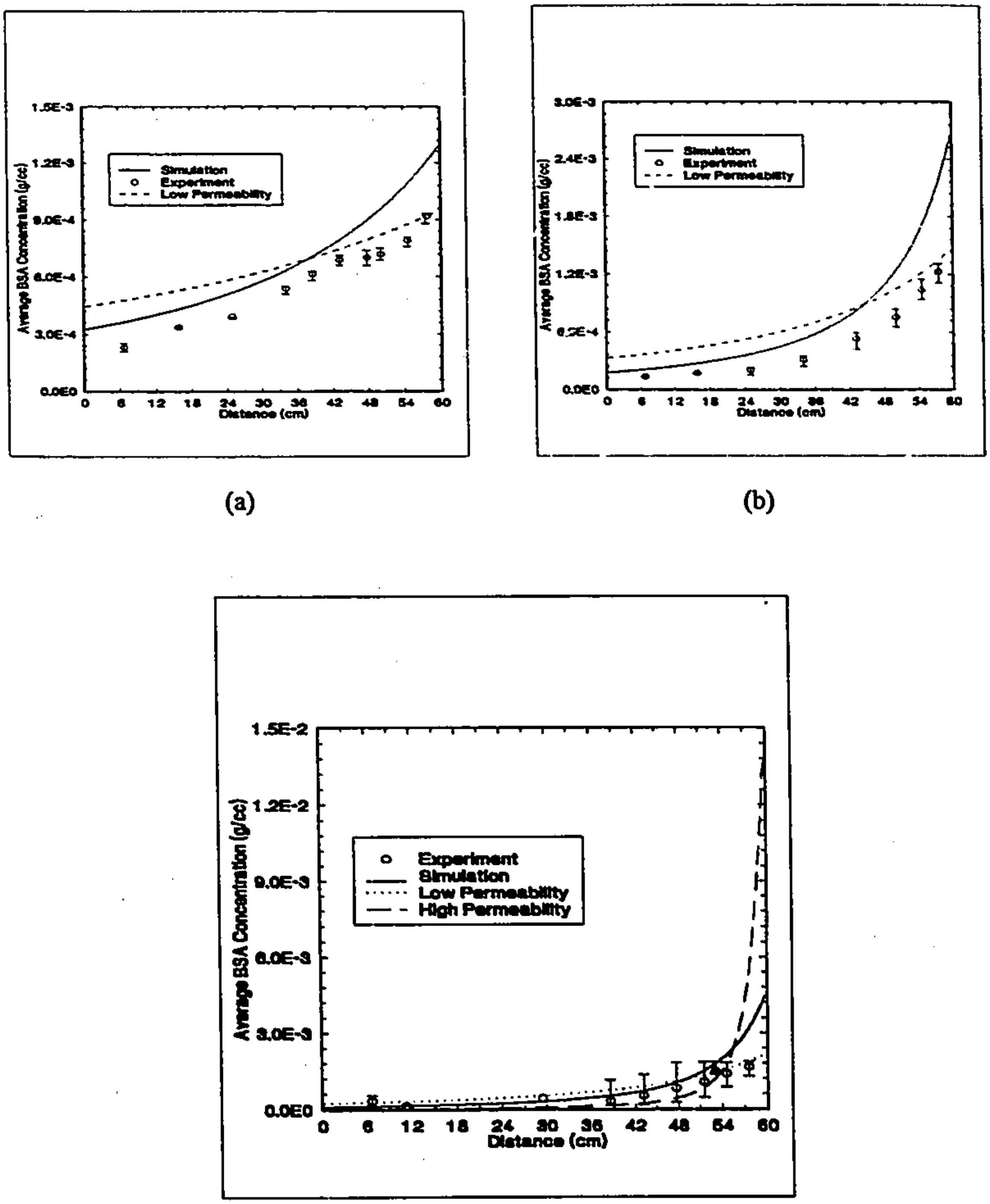

(a)

(b)

(c)

Figure 5.9. Plot illustrating the effect of membrane permeability on the theoretical concentration profiles of BSA following (a) 12 hours of operation (b) 24 hours of operation (c) 36 hours of operation. The low permeability is 1.96×10^{-11} m^2s/kg, the high permeability is 6.45×10^{-11} m^2s/kg and the average permeability is 3.63×10^{-11} m^2s/kg.

evidence shown in Figure 5.8 that the one-dimensional model is more accurate at low velocities. The major source of transverse polarization is the forced convection of protein to the membrane surface. This is further compounded by buoyancy effects that drive the protein to the membrane when the flow cell is operated in the horizontal position. The hydrated density of albumin is reported to be 1340 kg/m^3 by Vilker et al. (1981), which is substantially more dense than that of the phosphate buffer/sodium azide solution which was experimentally determined to be 999 kg/m^3. Therefore, buoyant forces could be responsible for further concentrating the protein layer at the membrane surface, leaving a protein-diluted solution within the sampling volume of the channel. Patkar et al. (1994) found that operation of the hollow fiber bioreactor in a vertical configuration seemed to eliminate natural convection effects due to density differences in the transverse direction. Therefore, the problem of diluted protein samples could possibly be alleviated by operating the rectilinear flow cell in a vertical orientation. Thirdly, given the local variability in the permeabilities of six coupons obtained from the original flat sheet membrane, the permeability should ideally be determined for the strip of membrane used in the flow cell. Therefore, characterization of the membrane strip, *in situ*, could be performed by collecting permeate from the lower chamber upon opening the bleed valve shown in Figure 3.1. The permeability evaluated from permeate samples obtained from the lower chamber would represent an average permeability of the membrane strip along the length of the chamber.

6. CONCLUSIONS AND RECOMMENDATIONS

6.1 Conclusions

1. Polarization of osmotically active bovine serum albumin was observed in the downstream region of a rectilinear flow cell operated with unidirectional flow.

2. The extent of albumin polarization increased with time. The downstream albumin concentration was 1.41, 1.78 and 2.24 times greater than the initial loading concentration in the upper chamber following 12, 24 and 36 hours of operation, respectively.

3. The concentration profiles predicted from theoretical analysis were strongly influenced by variations in L_p/μ over the range observed experimentally.

4. The cellulose acetate membrane was found to successfully retain BSA in the upper chamber of the rectilinear flow cell.

5. Albumin adsorption was observed on the membrane surface as indicated by a decrease in the membrane permeability.

6. Hysteresis in the membrane permeability was not observed upon increasing and decreasing the pressure drop across the membrane.

7. The BSA concentration profiles predicted from theoretical analysis over predicted the experimentally determined BSA concentration profiles. Experimental evidence suggested that the possibility of sedimentation and sample dilution were unlikely explanations for the observed discrepancy; however, transverse polarization, buoyancy effects, syringe

penetration depth and variability in membrane permeability are possible sources for the differences between theory and experimental results.

6.2 Recommendations

1. The rectilinear flow cell should be operated in the vertical orientation to limit the effects of buoyancy which may contribute to packing the protein at the membrane surface, as found by Patkar et al. (1994).

2. The mathematical model used to predict BSA concentration profiles should be modified from a one-dimensional model to a two-dimensional one in order to account for gradients in the transverse direction.

3. Other dilution techniques for analyzing BSA samples obtained from the flow cell should be explored; in particular, an appropriate column which is compatible with the Coomassie Blue dye should be found. Other dilution techniques would permit the withdrawal of smaller BSA samples from the flow cell.

4. The membrane permeability should be measured *in situ* by collecting permeate samples upon opening the bleed valve illustrated in Figure 3.1.

5. The steady-state polarization of albumin should be investigated.

6. The effect of sample syringe penetration depth on measured concentrations should be studied.

REFERENCES

Bailey, J.E. and Ollis, D.F., *Biochemical Engineering Fundamentals*, Second Edition, Chapter 7, McGraw-Hill Publishing Company, Montreal (1986).

Baker, R.W., "Membrane and Module Preparation" in *Membrane Separation Systems; Recent Developments and Future Directions*, 2, 100-150, Noyes Data Corp., New Jersey (1991).

Belfort, G., "Membranes and Reactors: A Technical Challenge in Biotechnology", *Biotechnology and Bioengineering*, 33, 1047-1066 (1989).

Bruining, W.J., "A General Description of Flows and Pressures in Hollow Fiber Membrane Modules", *Chemical Engineering Science*, 44, 1441-1447 (1989).

Bull, A.T., "Biotechnology: Opportunities and Constraints" in *Perspectives in Biotechnology*, Duarte, J.M.C., Archer, L.J., Bull, A.T. and Holt, G., Ed., 1-10, Plenum Press, New York (1987).

Burden, R.L., Faires, J.D. and Reynolds, A.C., *Numerical Analysis*, Second Edition, Ch. 10, Prindle, Webber and Schmidt, Boston (1981).

Cherry, R.S., "Oxygen Transport in Animal Cell Bioreactors" in *Chemical Engineering Problems in Biotechnology*, Shuler, M.L., Ed., 1, 107-128, American Institute of Chemical Engineers, New York (1989).

Harbour, C., Barford, J.P. and Low, K.S., "Process Development for Hybridoma Cells" in

Advances in Biochemical Engineering/Biotechnology, **37**, 2-37, Springer-Verlag (1988).

Heath, C. and Belfort, G., "Immobilization of Suspended Mammalian Cells: Analysis of Hollow Fiber and Microcapsule Bioreactors", *Advances in Biochemical Engineering/Biotechnology*, **34**, 1-31 (1987).

Heath, C.A., Belfort, G., Hammer, B.E., Mirer, S.D. and Pimbley, J.M., "Magnetic Resonance Imaging and Modeling of Flow in Hollow Fiber Bioreactors", *American Iinstitute of Chemical Engineers Journal*, **4**, 547-558 (1990).

Kelsey, L.J., Pillarella, M.R. and Zydney, A.L., "Theoretical Analysis of Convective Flow Profiles in a Hollow Fiber Membrane Bioreactor", *Chemical Engineering Science*, **45**, 3211-3220 (1990).

Leonard, E.F., "The Application of Artificial Organs to Biotechnology" in *Membane Separations in Biotechnology*, McGregor, W.C., Ed., Chap. 12, Marcel Dekker, Inc., New York (1986).

Libicki, S.B., Salmon, P.M. and Robertson, C.R., "The Effective Diffusive Permeability of a Nonreacting Solute in Microbial Cell Aggregates", *Biotechnology and Bioengineering*, **32**, 68-85 (1988).

Nabetani, H., Nakajima, M., Watanabe, A., Nakao, S. and Kimura, S., "Effects of Osmotic Pressure and Adsorption on Ultrafiltration of Ovalbumin", *American Institute of Chemical Engineers Journal*, **36**, 907-915 (1990).

Novais, J.M., "Immobilized Cell Systems for Energy Production" in *Perspectives in*

Biotechnology, Duarte, J.M.C., Archer, L.J., Bull, A.T. and Holt, G., Ed., 11-21, Plenum Press, New York (1987).

Othmer, K., *Encyclopedia of Chemical Technology*, Third Edition, 2, 871, Wiley-Interscience (1978).

Park, J.K., Chang, H.N., "Flow Distribution in the Fiber Lumen Side of a Hollow Fiber Module", *American Iinstitute of Chemical Engineers Journal*, **32**, 1937-1947 (1986).

Patankar, S.V., *Numerical Heat Transfer and Fluid Flow*, Chap. 4-5, Hemisphere Publishing Corp., New York (1980).

Patkar, A.Y., Koska, J., Taylor, D.G., Bowen, B.D. and Piret, J.M., "Experimental and Modeling Study of Hollow Fiber Bioreactor Protein Distributions", in print, *American Institute of Chemical Engineers Journal* (1994).

Pillarella, M.R. and Zydney, A.L., "Theoretical Analysis of the Effect of Convective Flow on Solute Transport and Insulin Release in a Hollow Fiber Bioartificial Pancreas", *Journal of Biochemical Engineering*, **112**, 220-228 (1990).

Piret, J.M. and Cooney, C.L., "Immobilized Mammalian Cell Cultivation in Hollow Fiber Bioreactors", *Biotechnology Advances*, **8**, 763-783 (1990a).

Piret, J.M. and Cooney, C.L., "Mammalian Cell and Protein Distributions in Ultrafiltration Hollow Fiber Bioreactors", *Biotechnology and Bioengineering*, **36**, 902-910 (1990b).

Piret, J.M. and Cooney, C.L., "Model of Oxygen Transport Limitations in Hollow Fiber

Bioreactors", *Biotechnology and Bioengineering*, **37**, 80-92 (1991).

Piret, J.M., Devens, D.A. and Cooney, C.L., "Nutrient and Metabolite Gradients in Mammalian Cell Hollow Fiber Bioreactors", *The Canadian Journal of Chemical Engineering*, **69**, 421-428 (1991).

Prokop, A., and Rosenberg, M.Z., "Bioreactor for Mammalian Cell Culture" *Advances in Biochemical Engineering/Biotechnology*, **39**, 30-69, Springer-Verlag (1989).

Schonberg, J.A. and Belfort, G., "Enhanced Nutrient Transport in Hollow Fiber Perfusion Bioreactors: A Theoretical Analysis", *Biotechnology Progress*, **3**, 80-89 (1987).

Shen, J.J.S. and Probstein, R.F., "On the Prediction of Limiting Flux in Laminar Ultrafiltration of Macromolecular Solutions", *Industrial Engineering Chemistry Fundamentals*, **16**, 459-465 (1977).

Taylor, D.G., Piret, J.M. and Bowen, B.D., "Protein Polarization in Isotropic Membrane Hollow Fiber Bioreactors", *American Instititue of Chemical Engineers Journal*, **40**, 321-333 (1994).

Tharakan, J.P. and Chau, P.C., "Operation and Pressure Distribution of Immobilized Cell Hollow Fiber Bioreactors", *Biotechnology and Bioengineering*, **28**, 1064-1071 (1986).

Vilker, V.L., Colton, C.K. and Smith, K.A., "The Osmotic Pressure of Concentrated Protein Solutions: Effect of Concentration and pH in Saline Solutions of Bovine Serum Albumin", *Journal of Colloid and Interface Science*, **79**, 548-565 (1981).

Vilker, V.L., Colton, C.K., Smith, K.A. and Green, D.L., "The Osmotic Pressure of Concentrated Protein and Lipoprotein Solutions and its Significance to Ultrafiltration", *Journal of Membrane Science*, **20**, 63-77 (1984).

Wales, M., "Pressure Drop Across Polarization Layers in Ultrafiltration", *American Chemical Society Symposium Series: Synthetic Membranes*, **1**, 162-169 (1981).

Waterland, L.R., Robertson, C.R. and Michaels, A.S., "Enzymatic Catalysis Using Asymmetric Hollow Fiber Membranes", *Chemical Engineering Communications*, **2**, 37-47 (1975).

Wijmans, J.G., Nakao, S., Van Den Berg, J.W.A., Troelstra, F.R. and Smolders, C.A., "Hydrodynamic Resistance of Concentration Polarization Boundary Layers in Ultrafiltration", *Journal of Membrane Science*, **22**, 117-135 (1985).

White, F.M., *Viscous Fluid Flow*, Second Edition, Chapter 3, McGraw-Hill, Inc., Montreal (1991).

APPENDIX A: POLARIZATION STUDY

This appendix contains the experimental data illustrating the transient polarization of BSA following 12, 24 and 36 hours of operation. The experimental data were used to construct the BSA concentration profile along the length of the rectilinear flow cell.

Table A.1. Average BSA concentrations after 12 hours of operation with an initial loading concentration of 6.50×10^{-1} ($\pm1.07\times10^{-2}$) kg/m^3 and a fluid velocity in the lower chamber of 0.12 m/s.

Sample Port	Distance, m	Concentration, kg/m^3
2	0.0680	0.230 (±0.021)
4	0.1580	0.336 (±0.057)
6	0.2492	0.392 (±0.099)
8	0.3404	0.539 (±0.025)
9	0.3860	0.615 (±0.024)
10	0.4316	0.689 (±0.041)
12	0.4776	0.701 (±0.038)
13	0.5006	0.719 (±0.036)
16	0.5456	0.791 (±0.026)
18	0.5756	0.919 (±0.033)

Table A.2. Average BSA concentrations after 24 hours of operation with an initial loading concentration of 6.91×10^{-1} ($\pm4.91\times10^{-2}$) kg/m^3 and a fluid velocity in the lower chamber of 0.12 m/s.

Sample Port	Distance, m	Concentration, kg/m^3
2	0.0680	0.136 (±0.014)
4	0.1580	0.172 (±0.005)
6	0.2492	0.204 (±0.046)
8	0.3404	0.309 (±0.058)
10	0.4316	0.529 (±0.092)
13	0.5006	0.755 (±0.097)
16	0.5456	1.036 (±0.107)
18	0.5756	1.228 (±0.100)

Table A.3. Average BSA concentrations after 36 hours of operation with an initial loading concentration of 7.45×10^{-1} ($\pm7.44\times10^{-2}$) kg/m^3 and a fluid velocity in the lower chamber of 0.12 m/s.

Sample Port	Distance, m	Concentration, kg/m^3
2	0.0680	0.347 (±0.290)
3	0.1124	0.143 (±0.0)
7	0.2948	0.332 (±0.0)
9	0.3860	0.436 (±0.421)
10	0.4316	0.549 (±0.547)
12	0.4776	0.829 (±0.694)
14	0.5156	1.070 (±0.589)
15	0.5306	1.475 (±0.366)
16	0.5456	1.410 (±0.393)
18	0.5756	1.665 (±0.256)

The following tables contain experimental data obtained in the investigation of the discrepancy observed between the theoretical and experimental BSA concentration profiles. To this end, the following polarization experiments were conducted to study possible dilution of the BSA samples: the outlet valve on the upper chamber was opened during sampling and the corresponding BSA concentration profile is shown in Figure A.1; four BSA samples were obtained from the flow cell, rather than the usual 8 to 10. In addition, the assumption of a one dimensional model was investigated at a low luminal velocity.

Table A.4. Average BSA concentrations after 12 hours of operation with an initial loading concentration of 7.44×10^{-1} kg/m^3, a fluid velocity in the lower chamber of 0.12 m/s and with the inlet and outlet valves to the upper chamber open during sampling.

Sample Port	Distance, m	Concentration, kg/m^3
2	0.0680	0.234
4	0.1580	0.349
6	0.2492	0.419
8	0.3404	0.581
9	0.3860	0.624
10	0.4316	0.764
13	0.5006	0.821
16	0.5456	0.916
18	0.5756	1.041

Table A.5. Average BSA concentrations after 12 hours of operation with an initial loading concentration of 7.01×10^{-1} ($\pm2.83\times10^{-3}$) kg/m^3, a fluid velocity in the lower chamber of 0.12 m/s and with four sampling ports.

Sample Port	Distance, m	Concentration, kg/m^3
2	0.0680	0.224 (±0.018)
6	0.2492	0.399 (±0.071)
10	0.4316	0.692 (±0.068)
18	0.5756	1.013 (±0.028)

Table A.6. Average BSA concentrations after 48 hours of operation with an initial loading concentration of 5.47×10^{-1} ($\pm2.17\times10^{-2}$) kg/m^3 and a fluid velocity in the lower chamber of 0.02 m/s.

Sample Port	Distance, m	Concentration, kg/m^3
3	0.1124	0.452 (±0.029)
5	0.2036	0.455 (±0.016)
6	0.2492	0.531 (±0.067)
8	0.3404	0.611 (±0.083)
10	0.4316	0.665 (±0.058)
12	0.4776	0.642 (±0.062)
15	0.5306	0.699 (±0.043)
18	0.5756	0.668 (±0.014)

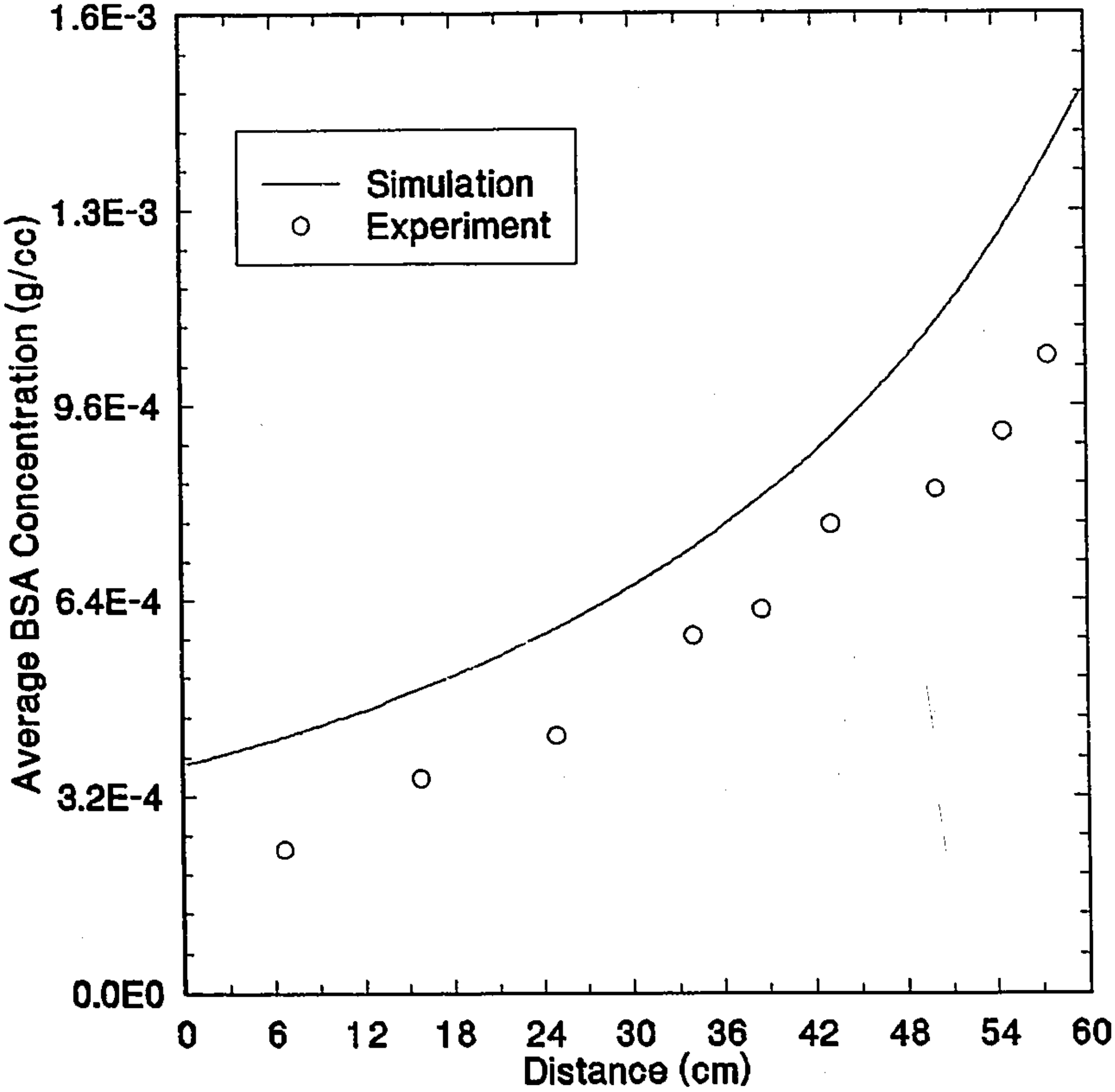

Figure A.1. Transient concentration profile of BSA following 12 hours of operation with the inlet and outlet valves to the upper chamber opened, $C_{io} = 7.44\times10^{-1}$ kg/m^3 and $\overline{u}_L = 0.12$ m/s.

APPENDIX B: MEMBRANE CHARACTERIZATION

Characterization of the cellulose acetate membrane used in the rectilinear flow cell was performed to obtain a measure of the membrane permeability. The following experimental data were collected to investigate the following: hysteresis of the membrane permeability as the pressure is increased and subsequently decreased; the effect of BSA binding on the membrane permeability; and the effects of aging on the membrane permeability. The quantity L_p/μ tabulated in the Results Section was calculated by obtaining the slope from a linear regression of the following data and dividing by the cross-sectional area of the coupon. The cross-sectional areas of coupons 1, 2, 3, 4, 5 and 6 are: 1.425×10^{-3}, 1.425×10^{-3} 1.605×10^{-3}, 1.486×10^{-3}, 1.59×10^{-3} and 1.633×10^{-3} m^2, respectively. A sample calculation of the pressure drop across a coupon will now be shown for coupon 1, with deionized water as the feed. The experimental results for this sample calculation appear in Table B.1.

P_{in} = 105218 Pa and P_{out} = 103287 Pa, as shown in Figure 3.3.

Overall pressure drop across the three test flow cells = $P_{in} - P_{out} = \Delta P = 1931$ Pa.

For three test flow cells at the same height, the overall pressure drop may be divided by three to yield the pressure drop across each individual flow cell. Therefore, the outlet pressure to the first flow cell containing coupon 1 is given by

$$\text{Pin} - \Delta P/3 = 105218 - (1931/3) = 104574 \text{ Pa.}$$

The pressure drop across coupon 1 is taken as the average of the inlet and oulet pressures to the first test flow cell: (105218 + 104574)/2 = 104896. Adjusting for atmospheric pressure yields 4367 Pa.

Table B.1. The experimental data used to construct plots of permeation rate versus pressure drop across the membrane coupon 1.

Coupon	Inlet Pressure, Pa (psia)	Outlet Pressure, Pa (psia)	Atmospheric Pressure, Pa (psia)	Average Permeation Rate, mL/hr	Pressure Drop Across Coupon, Pa (psi)
Permeation rate data obtained with deionized water					
1	105218 (15.26)	103287 (14.98)	100528 (14.58)	2.05 (±0.006)	4367 (0.63)
	110527 (16.03)	108458 (15.73)	101554 (14.73)	3.61 (±0.0)	8619 (1.25)
	124662 (18.08)	122248 (17.73)	101554 (14.73)	9.70 (±0.006)	22696 (3.29)
	138038 (20.02)	136314 (19.77)	101834 (14.77)	15.20 (±0.0)	35911 (5.21)
Permeation rate data for hysteresis experiments with deionized water					
	124593 (18.07)	122524 (17.77)	101834 (14.77)	9.61 (±0.006)	22409 (3.25)
	109837 (15.93)	107769 (15.63)	100861 (14.63)	3.65 (±0.040)	8619 (1.25)
	105562 (15.31)	103632 (15.03)	100861 (14.63)	1.90 (±0.0)	4367 (0.63)
Permeation rate data obtained with a solution of phosphate buffer/sodium azide					
	105356(15.28)	103356(14.99)	100568(14.59)	1.90 (±0.0)	4424 (0.64)
	109837(15.93)	107493(15.59)	100568(14.59)	3.80 (±0.087)	8849 (1.28)
	121697(17.65)	119352(17.31)	98689(14.31)	9.32 (±0.0)	22639 (3.28)
	135142(19.60)	133142(19.31)	98689(14.31)	14.50 (±0.0)	36141 (5.24)
Permeation rate data for protein binding experiments					
	106666 (15.47)	104804 (15.20)	102034 (14.80)	1.43 (±0.029)	4309 (0.62)
	118249 (17.15)	115836 (16.80)	102034 (14.80)	5.42 (±0.072)	15801 (2.29)
	138658 (20.11)	133074 (19.30)	102260 (14.83)	11.97 (±0.153)	36084 (5.23)
Permeation rate data for hysteresis experiments following protein binding					
	118663 (17.21)	116043 (16.83)	102260 (14.83)	5.46 (±0.052)	15973 (2.32)
	106735 (15.48)	104115 (15.10)	101328 (14.70)	1.75 (±0.0)	4941 (0.72)
Permeation rate data for aging experiments					
	105769 (15.34)	102046 (14.80)	101962 (14.60)	0.52 (±0.0)	3914 (0.57)
	110113 (15.97)	107562 (15.60)	101962 (14.60)	3.05 (±0.0)	8709 (1.26)
	123972 (17.98)	121214 (17.58)	101826 (14.58)	7.75 (±0.0)	22800 (3.31)
	137417 (19.93)	135004 (19.58)	101826 (14.58)	12.71 (±0.115)	36535 (5.30)

Table B.2 The experimental data used to construct plots of permeation rate versus pressure drop across the membrane coupon 2

Coupon	Inlet Pressure, Pa (psia)	Outlet Pressure, Pa (psia)	Atmospheric Pressure, Pa (psia)	Average Permeation Rate, mL/hr	Pressure Drop Across Coupon, Pa (psi)
Permeation rate data obtained with deionized water					
2	105218 (15.26)	103287 (14.98)	100528 (14.58)	0.81 (±0.0)	3723 (0.54)
	110527 (16.03)	108458 (15.73)	101554 (14.73)	2.00 (±0.0)	7929 (1.15)
	124662 (18.08)	122248 (17.73)	101554 (14.73)	5.50 (±0.0)	21892 (3.18)
	138038 (20.02)	136314 (19.77)	101834 (14.77)	8.63 (±0.046)	35337 (5.13)
Permeation rate data for hysteresis experiments with deionized water					
	124593 (18.07)	122524 (17.77)	101834 (14.77)	5.43 (±0.036)	21719 (3.15)
	109837 (15.93)	107769 (15.63)	100861 (14.63)	2.03 (±0.029)	7929 (1.15)
	105562 (15.31)	103632 (15.03)	100861 (14.63)	1.01 (±0.012)	3723 (0.54)
Permeation rate data obtained with a solution of phosphate buffer/sodium azide					
	105356(15.28)	103356(14.99)	100568(14.59)	0.98 (±0.0)	3758 (0.55)
	109837(15.93)	107493(15.59)	100568(14.59)	2.06 (±0.052)	8067 (1.17)
	121697(17.65)	119352(17.31)	98689(14.31)	5.20 (±0.0)	21857 (3.17)
	135142(19.60)	133142(19.31)	98689(14.31)	8.09 (±0.036)	35475 (5.15)
Permeation rate data for protein binding experiments					
	106666 (15.47)	104804 (15.20)	102034 (14.80)	0.71 (±0.012)	3689 (0.54)
	118249 (17.15)	115836 (16.80)	102034 (14.80)	2.97 (±0.061)	14997 (2.18)
	138658 (20.11)	133074 (19.30)	102260 (14.83)	6.78 (±0.076)	35440 (5.14)
Permeation rate data for hysteresis experiments following protein binding					
	118663 (17.21)	116043 (16.83)	102260 (14.83)	3.00 (±0.055)	15100 (2.19)
	106735 (15.48)	104115 (15.10)	101328 (14.70)	0.90 (±0.006)	4068 (0.59)
Permeation rate data for aging experiments					
	105769 (15.34)	102045 (14.80)	101962 (14.60)	1.00 (±0.006)	2655 (0.39)
	110113 (15.97)	107562 (15.60)	101962 (14.60)	2.13 (±0.029)	7847 (1.14)
	123972 (17.98)	121214 (17.58)	101826 (14.58)	5.37 (±0.115)	21869 (3.17)
	137417 (19.93)	135004 (19.58)	101826 (14.58)	9.07 (±0.115)	35721 (5.18)

Table B.3. The experimental data used to construct plots of permeation rate versus pressure drop across the membrane coupon 3.

Coupon	Inlet Pressure, Pa (psia)	Outlet Pressure, Pa (psia)	Atmospheric Pressure, Pa (psia)	Average Permeation Rate, mL/hr	Pressure Drop Across Coupon, Pa (psi)
Permeation rate data obtained with deionized water					
3	105218 (15.26)	103287 (14.98)	100528 (14.58)	1.06 (±0.046)	3080 (0.45)
	110527 (16.03)	108458 (15.73)	101554 (14.73)	2.41 (±0.0)	7240 (1.05)
	124662 (18.08)	122248 (17.73)	101554 (14.73)	6.90 (±0.0)	21087 (3.06)
	138038 (20.02)	136314 (19.77)	101834 (14.77)	11.00 (±0.0)	34762 (5.04)
Permeation rate data for hysteresis experiments with deionized water					
	124593 (18.07)	122524 (17.77)	101834 (14.77)	6.85 (±0.050)	21030 (3.05)
	109837 (15.93)	107769 (15.63)	100861 (14.63)	2.52 (±0.035)	7240 (1.05)
	105562 (15.31)	103632 (15.03)	100861 (14.63)	1.22 (±0.0)	3080 (0.45)
Permeation rate data obtained with a solution of phosphate buffer/sodium azide					
	105356(15.28)	103356(14.99)	100568(14.59)	1.15 (±0.0)	3091 (0.45)
	109837(15.93)	107493(15.59)	100568(14.59)	2.51 (±0.032)	7286 (1.06)
	121697(17.65)	119352(17.31)	98689(14.31)	6.50 (±0.0)	21076 (3.06)
	135142(19.60)	133142(19.31)	98689(14.31)	10.10 (±0.10)	34808 (5.05)
Permeation rate data for protein binding experiments					
	106666 (15.47)	104804 (15.20)	102034 (14.80)	0.81 (±0.0)	3068 (0.44)
	118249 (17.15)	115836 (16.80)	102034 (14.80)	3.62 (±0.075)	14192 (2.06)
	138658 (20.11)	133074 (19.30)	102260 (14.83)	8.42 (±0.025)	34797 5.05)
Permeation rate data for hysteresis experiments following protein binding					
	118663 (17.21)	116043 (16.83)	102260 (14.83)	3.71 (±0.090)	14227 (2.06)
	106735 (15.48)	104115 (15.10)	101328 (14.70)	1.05 (±0.0)	3195 (0.46)
Permeation rate data for aging experiments					
	105769 (15.34)	102046 (14.80)	101962 (14.60)	0.87 (±0.029)	1398 (0.20)
	110113 (15.97)	107562 (15.60)	101962 (14.60)	2.05 (±0.0)	6985 (1.01)
	123972 (17.98)	121214 (17.58)	101826 (14.58)	5.85 (±0.006)	20952 (3.04)
	137417 (19.93)	135004 (19.58)	101826 (14.58)	9.72 (±0.029)	34920 (5.06)

Table B.4. The experimental data used to construct plots of permeation rate versus pressure drop across the membrane coupon 4. The following data were obtained using deionized water.

Coupon	Inlet Pressure, Pa (psia)	Outlet Pressure, Pa (psia)	Atmospheric Pressure, Pa (psia)	Average Permeation Rate, mL/hr	Pressure Drop Across Coupon, Pa (psi)
Permeation rate data obtained with deionized water					
4	103839 (15.06)	102667 (14.89)	101261 (14.69)	0.52 (±0.0)	2356 (0.34)
	105218 (15.26)	104046 (15.09)	101261 (14.69)	0.85 (±0.0)	3735 (0.54)
	106735 (15.48)	105356 (15.28)	101234 (14.68)	1.20 (±0.006)	5286 (0.77)
	110182 (15.98)	108114 (15.68)	101234 (14.68)	1.96 (±0.023)	8619 (1.25)
	116526 (16.90)	114112 (16.55)	100341 (14.55)	3.25 (±0.050)	15801 (2.29)
	124179 (18.01)	121007 (17.55)	100341 (14.55)	5.00 (±0.0)	23328 (3.38)
	130384 (18.91)	128040 (18.57)	100448 (14.57)	6.22 (±0.038)	29534 (4.28)
	136659 (19.82)	134935 (19.57)	100448 (14.57)	7.55 (±0.046)	35911 (5.21)
Permeation rate data for hysteresis experiments					
	123834 (17.96)	121559 (17.63)	100861 (14.63)	4.66 (±0.081)	22581 (3.27)
	109424 (15.87)	107769 (15.63)	100861 (14.63)	1.65 (±0.0)	8274 (1.20)
	107217 (15.55)	105561 (15.31)	101394 (14.71)	1.10 (±0.0)	5516 (0.80)
	104666 (15.18)	102804 (14.91)	101394 (14.71)	0.60 (±0.0)	2930 (0.42)
Permeation rate data for protein binding experiments					
	105631 (15.32)	104390 (15.14)	101621 (14.74)	0.50 (±0.012)	3792 (0.55)
	117905 (17.10)	115422 (16.74)	101621 (14.74)	2.20 (±0.0)	15859 (2.30)
	137279 (19.91)	135556 (19.66)	101074 (14.66)	5.23 (±0.059)	35911 (5.21)
Permeation rate data for hysteresis experiments following protein binding					
	117146 (16.99)	114871 (16.66)	101074 (14.66)	2.32 (±0.035)	15686 (2.27)
	105218 (15.26)	103287 (14.98)	100528 (14.58)	0.63 (±0.0)	4367 (0.63)

Table B.5. The experimental data used to construct plots of permeation rate versus pressure drop across the membrane coupon 5. The following data were obtained using deionized water.

Coupon	Inlet Pressure, Pa (psia)	Outlet Pressure, Pa (psia)	Atmospheric Pressure, Pa (psia)	Average Permeation Rate, mL/hr	Pressure Drop Across Coupon, Pa (psi)
Permeation rate data obtained with deionized water					
5	103839 (15.06)	102667 (14.89)	101261 (14.69)	0.45 (±0.0)	1965 (0.28)
	105218 (15.26)	104046 (15.09)	101261 (14.69)	0.80 (±0.0)	3344 (0.48)
	106735 (15.48)	105356 (15.28)	101234 (14.68)	1.20 (±0.0)	4827 (0.70)
	110182 (15.98)	108114 (15.68)	101234 (14.68)	1.97 (±0.029)	7929 (1.15)
	116526 (16.90)	114112 (16.55)	100341 (14.55)	3.26 (±0.071)	14997 (2.18)
	124179 (18.01)	121007 (17.55)	100341 (14.55)	5.11 (±0.012)	22271 (3.23)
	130384 (18.91)	128040 (18.57)	100448 (14.57)	6.34 (±0.075)	28752 (4.17)
	136659 (19.82)	134935 (19.57)	100448 (14.57)	7.78 (±0.104)	35337 (5.13)
Permeation rate data for hysteresis experiments					
	123834 (17.96)	121559 (17.63)	100861 (14.63)	4.73 (±0.058)	21823 (3.17)
	109424 (15.87)	107769 (15.63)	100861 (14.63)	1.64 (±0.006)	7722 (1.12)
	107217 (15.55)	105561 (15.31)	101394 (14.71)	1.05 (±0.0)	4964 (0.72)
	104666 (15.18)	102804 (14.91)	101394 (14.71)	0.55 (±0.012)	2310 (0.36)
Permeation rate data for protein binding experiments					
	105631 (15.32)	104390 (15.14)	101621 (14.74)	0.53 (±0.0)	3379 (0.49)
	117905 (17.10)	115422 (16.74)	101621 (14.74)	2.40 (±0.006)	15031 (2.18)
	137279 (19.91)	135556 (19.66)	101074 (14.66)	5.56 (±0.046)	35337 (5.13)
Permeation rate data for hysteresis experiments following protein binding					
	117146 (16.99)	114871 (16.66)	101074 (14.66)	2.48 (±0.026)	14928 (2.17)
	105218 (15.26)	103287 (14.98)	100528 (14.58)	0.63 (±0.0)	3723 (0.54)

Table B.6. The experimental data used to construct plots of permeation rate versus pressure drop across the membrane coupon 6. The following data were obtained using deionized water.

Coupon	Inlet Pressure, Pa (psia)	Outlet Pressure, Pa (psia)	Atmospheric Pressure, Pa (psia)	Average Permeation Rate, mL/hr	Pressure Drop Across Coupon, Pa (psi)
Permeation rate data obtained with deionized water					
6	103839 (15.06)	102667 (14.89)	101261 (14.69)	0.30 (±0.0)	1574 (0.23)
	105218 (15.26)	104046 (15.09)	101261 (14.69)	0.58 (±0.0)	2953 (0.43)
	106735 (15.48)	105356 (15.28)	101234 (14.68)	0.85 (±0.029)	4367 (0.63)
	110182 (15.98)	108114 (15.68)	101234 (14.68)	1.43 (±0.029)	7240 (1.05)
	116526 (16.90)	114112 (16.55)	100341 (14.55)	2.47 (±0.026)	14192 (2.06)
	124179 (18.01)	121007 (17.55)	100341 (14.55)	3.80 (±0.0)	21214 (3.08)
	130384 (18.91)	128040 (18.57)	100448 (14.57)	4.76 (±0.036)	27971 (4.06)
	136659 (19.82)	134935 (19.57)	100448 (14.57)	5.73 (±0.108)	34762 (5.04)
Permeation rate data for hysteresis experiments					
	123834 (17.96)	121559 (17.63)	100861 (14.63)	3.53 (±0.058)	21064 (3.05)
	109424 (15.87)	107769 (15.63)	100861 (14.63)	1.21 (±0.023)	7171 (1.04)
	107217 (15.55)	105561 (15.31)	101394 (14.71)	0.72 (±0.029)	4413 (0.64)
	104666 (15.18)	102804 (14.91)	101394 (14.71)	0.29 (±0.012)	1689 (0.24)
Permeation rate data for protein binding experiments					
	105631 (15.32)	104390 (15.14)	101621 (14.74)	0.35 (±0.0)	2965 (0.43)
	117905 (17.10)	115422 (16.74)	101621 (14.74)	1.69 (±0.012)	14204 (2.06)
	137279 (19.91)	135556 (19.66)	101074 (14.66)	4.02 (±0.029)	34762 (5.04)
Permeation rate data for hysteresis experiments following protein binding					
	117146 (16.99)	114871 (16.66)	101074 (14.66)	1.79 (±0.025)	14169 (2.05)
	105218 (15.26)	103287 (14.98)	100528 (14.58)	0.48 (±0.0)	3080 (0.45)

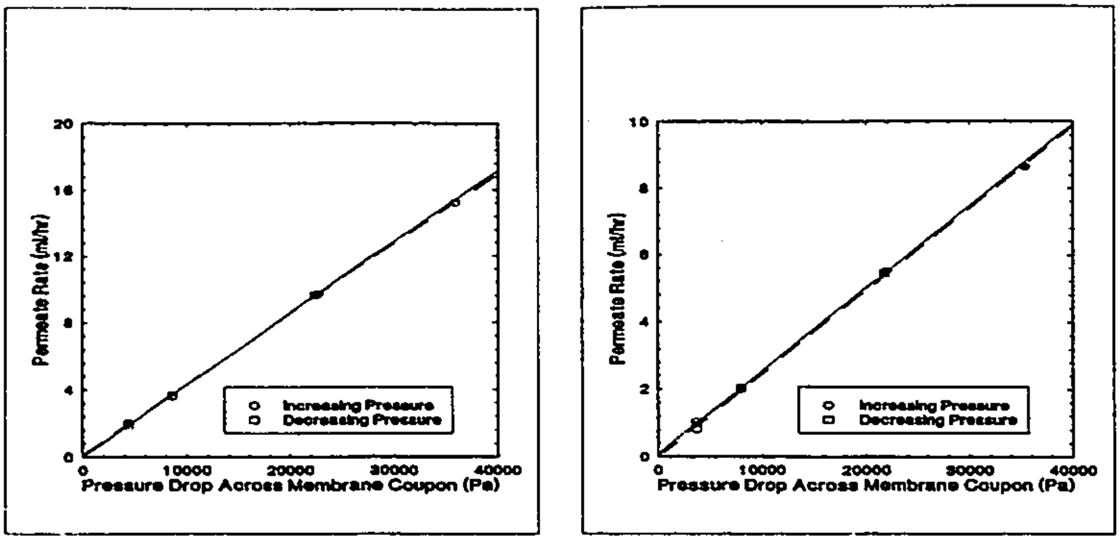

(a) Coupon 1

(b) Coupon 2

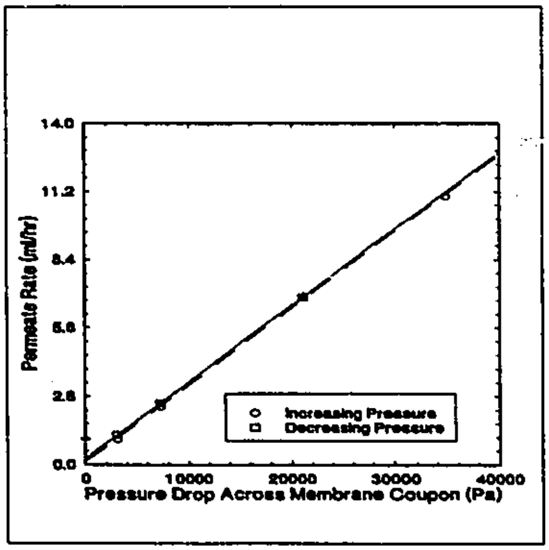

(c) Coupon 3

Figure B.1A. Plot of permeation rate data obtained with deionized water to investigate hysteresis in the membrane permeability due to increasing and decreasing pressures. The dashed lines denote data obtained with increasing pressures and the solid lines represent data obtained with decreasing pressures.

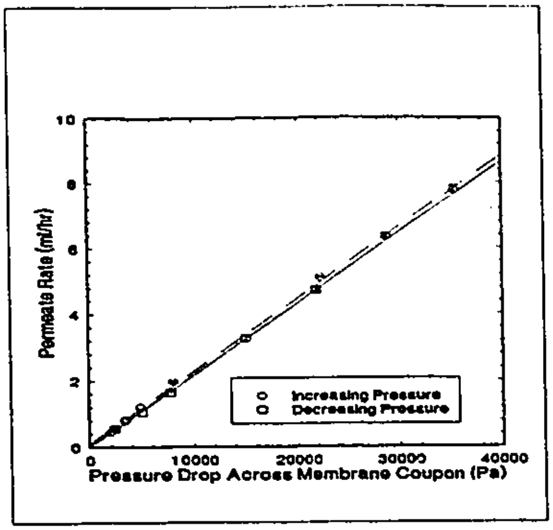

(a) Coupon 5

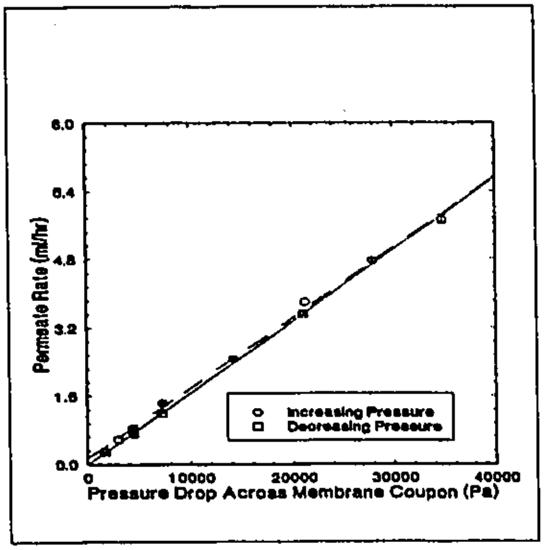

(b) Coupon 6

Figure B.1B. Plot of permeation rate data obtained with deionized water to investigate hysteresis in the membrane permeability due to increasing and decreasing pressures. The dashed lines denote data obtained with increasing pressures and the solid lines represent data obtained with decreasing pressures.

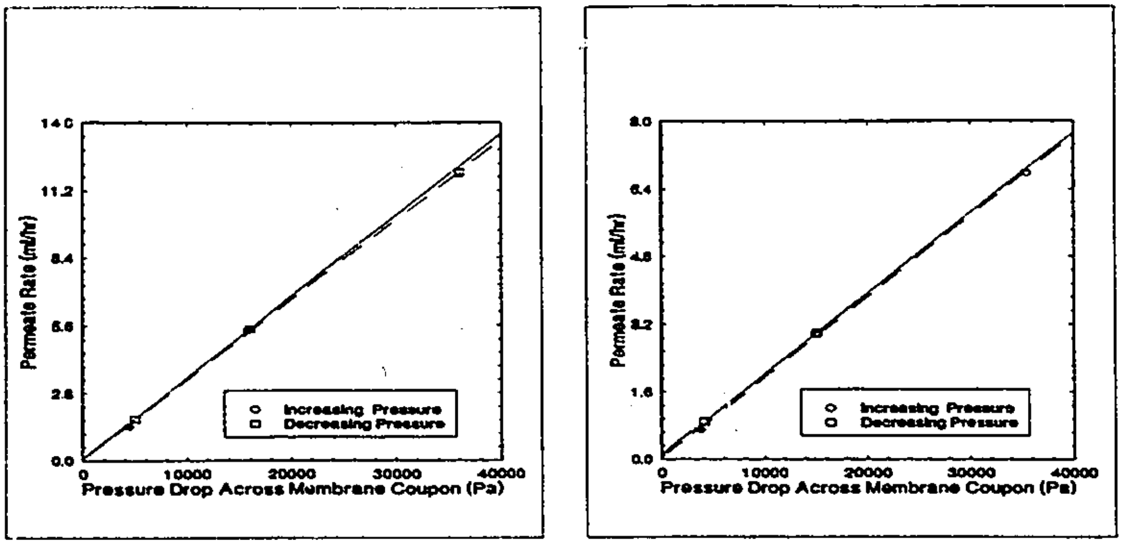

(a) Coupon 1

(b) Coupon 2

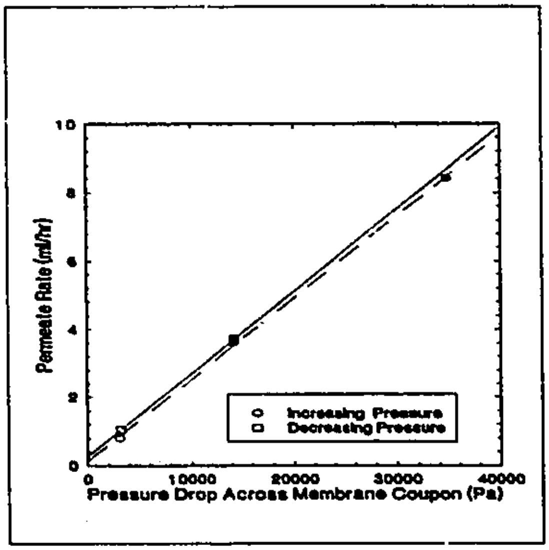

(c) Coupon 3

Figure B.2. Plots of permeation rate data with a solution of phosphate buffer and sodium azide to investigate hysteresis in the membrane permeability due to increasing and decreasing pressures. The dashed lines denote data obtained with increasing pressures and the solid lines represent data obtained with decreasing pressures.

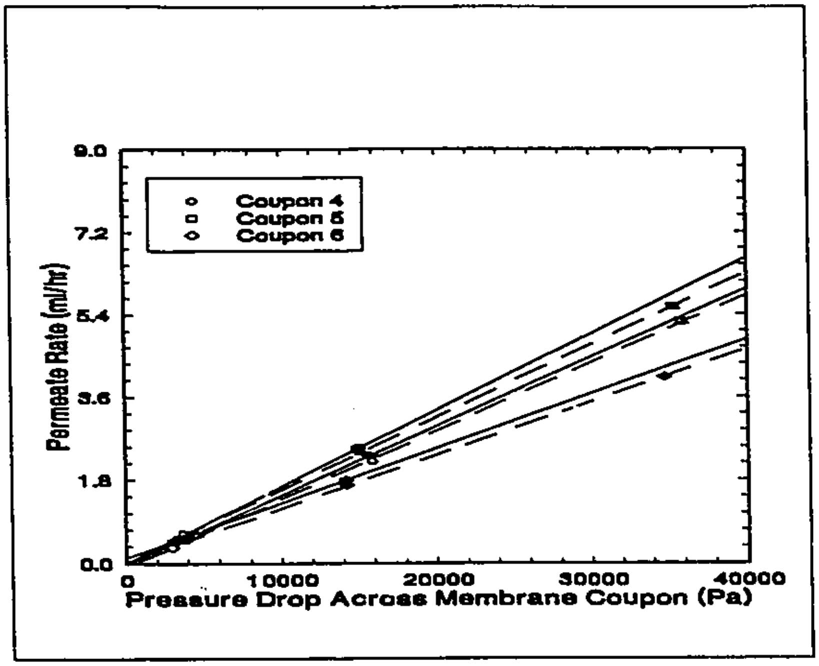

(a)

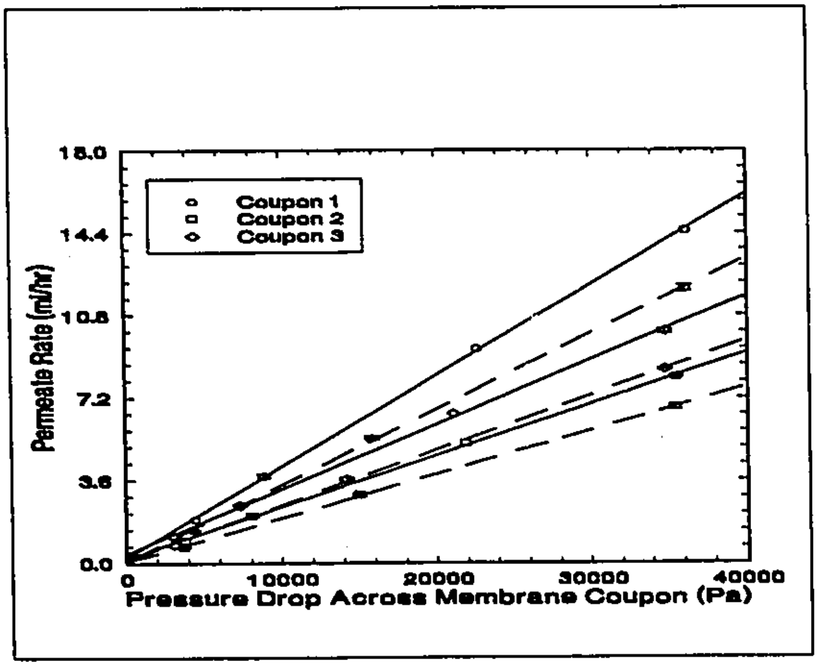

(b)

The dashed lines denote data obtained with increasing pressures and the solid lines represent data obtained with decreasing pressures. (b) Plot of permeation rate data obtained with a solution of phosphate buffer and sodium azide. The dashed lines denote data obtained following conditioning with BSA and the solid lines represent data obtained prior to conditioning of the membrane with BSA.

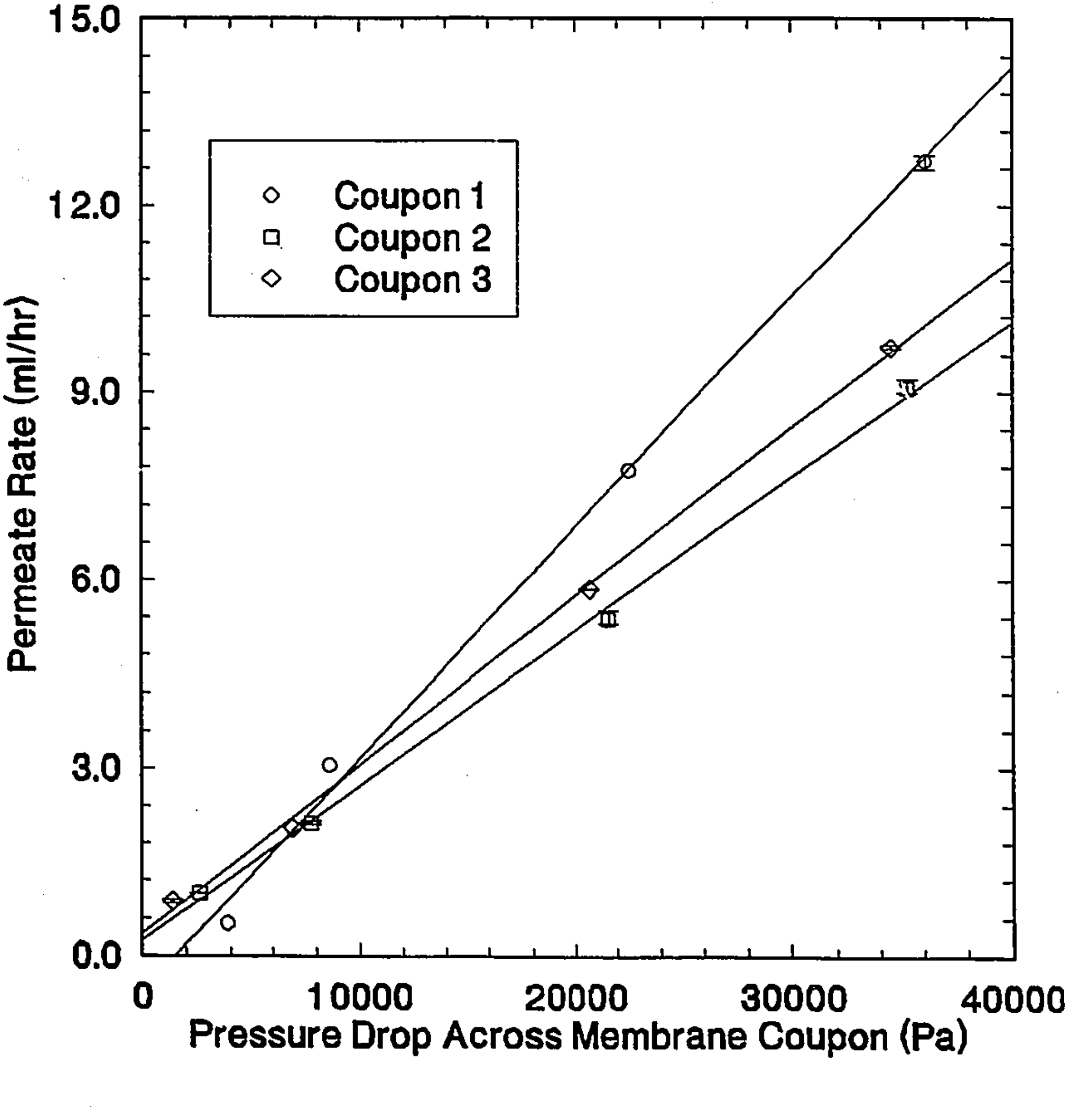

Figure B.4. Plot of permeation rate data obtained following storage of the membrane for 5 months in a solution of 0.5% v/v formaldehyde.